Systematic Evaluation of a Transformer-Based Surrogate for Distributed Groundwater Dynamics: Long-Horizon Prediction, Dynamic–Static Fusion, and Data Augmentation

Hui Huang[1], Aoqi Sun[1], Hoang Tran[2], Yongjiu Dai[1], Chen Yang[1]

[1]School of Atmospheric Sciences, Sun Yat-sen University, Zhuhai, China
[2]Atmospheric Science & Global Change Division, Pacific Northwest National Laboratory, Richland, WA, USA

*Correspondence to: Chen Yang (yangch329@mail.sysu.edu.cn)

Abstract

Transformers are increasingly reshaping artificial-intelligence-based Earth system prediction, yet their suitability for distributed groundwater surrogate modeling remains poorly understood. Groundwater dynamics combine strong temporal persistence with spatial interactions governed by heterogeneous hydrogeological conditions. These characteristics make attention-based architectures potentially well suited to representing the long-range spatiotemporal dependencies of groundwater systems, rather than merely providing an alternative to recurrent models. Here, we systematically evaluated a groundwater-adapted PredFormer as a surrogate for regional ParFlow-CLM simulations. The adapted model combined temporal-first factorized attention with pressure-residual prediction and blockwise autoregressive rollout. We assessed its long-horizon prediction behavior over 720 h, the contributions of prescribed P−ET (PME) forcing and static attributes, alternative static-fusion strategies, its performance relative to PredRNN, and precipitation-regime-specific data augmentation generated by perturbing precipitation forcing.

Over the horizon, the adapted PredFormer maintained decimeter-scale median water table depth (WTD) errors, although error magnitude varied among WTD regimes. Larger upper-tail spatial errors were associated with precipitation amount and variability, whereas temporal fluctuations in the error trajectories were more closely associated with abrupt wet–dry transitions. Adding prescribed PME produced the largest and most consistent reduction in prediction error, although the benefits of dynamic and static inputs varied systematically with WTD. Post-temporal–spatial cross-attention performed best among the static-fusion strategies. PredRNN was more accurate initially, but PredFormer performed better at longer lead times and in most segments. Data augmentation produced modest overall changes but clear regime-dependent benefits when the added samples matched the precipitation conditions encountered during prediction.

These findings show that the advantages of Transformer-based groundwater surrogates emerge primarily over extended autoregressive horizons and depend on groundwater state, input composition, information-fusion strategy, and training-sample coverage. The results provide process-informed guidance for developing computationally efficient groundwater surrogates for regional prediction and water-resources management, while also highlighting their longer-term potential to provide AI-enabled representations of groundwater dynamics within Earth system models.

1. Introduction

Over the past several decades, continuous improvements in numerical weather prediction systems, data assimilation techniques, and global observation networks have produced massive, spatiotemporally consistent datasets, such as ERA5 and other global reanalysis products (Hersbach et al., 2020). The long-term accumulation of these high-quality numerical and observational datasets has provided abundant training data spanning diverse meteorological conditions, substantially accelerating the adoption of artificial intelligence in weather and climate prediction and enabling the development of increasingly powerful data-driven models (Bi et al., 2023; Kochkov et al., 2024; Sun et al., 2025). More recently, these developments have progressed toward Earth foundation models trained on heterogeneous Earth system datasets, marking a new stage in AI-driven Earth system modeling (Nguyen et al., 2023; Bodnar et al., 2025; Reichstein et al., 2019).

In comparison, groundwater modeling has historically been constrained by limited observations of subsurface hydraulic properties and groundwater states, making large-scale data-driven learning considerably more challenging (Taylor et al., 2012; Jesse et al., 2025). Nevertheless, increasing recognition of groundwater as an active component of the Earth system has led to substantial developments in continental- and global-scale integrated hydrological models during the past two decades (Yang et al., 2026b). Physically based models, such as ParFlow-CLM (Kollet and Maxwell, 2008) and other integrated groundwater-land surface modeling systems, have generated increasingly extensive spatiotemporal simulations of groundwater states, soil moisture, evapotranspiration, and surface water fluxes. Although these simulated datasets remain considerably smaller and less constrained than atmospheric reanalysis products, they nevertheless provide an emerging data source that enables the development of data-driven groundwater surrogate models.

Recent groundwater surrogate studies have demonstrated the feasibility of learning numerical model behavior using deep learning techniques (Li et al., 2025; Maxwell et al., 2021). Existing studies have primarily employed recurrent neural network (RNN)-based architectures, including LSTM, ConvLSTM, and PredRNN, to emulate groundwater dynamics or accelerate physically based simulations (Tran et al., 2021; Dai et al., 2025). More broadly, recurrent architectures continue to dominate many data-driven hydrological applications because of their ability to model temporal dependencies (Kratzert et al., 2018; Liu et al., 2025). However, recent developments in artificial intelligence have increasingly shifted toward Transformer-based architectures (Vaswani et al., 2017), which have shown remarkable success across computer vision (Dosovitskiy et al., 2020), natural language processing, and, more recently, Earth system modeling (Gao et al., 2022). Compared with recurrent models, Transformers provide a fundamentally different mechanism for capturing long-range dependencies through self-attention rather than sequential state propagation. While Transformer-based models have begun to emerge in hydrological prediction, recent benchmarking studies suggest that no single architecture consistently outperforms others across different hydrological tasks and datasets (Rasiya Koya and Roy, 2024; Dai et al., 2025). For distributed groundwater surrogate modeling, where long-term memory, strong spatial heterogeneity, and complex groundwater-land surface interactions coexist, the applicability of Transformer architectures remains largely unexplored (Jesse et al., 2025).

To realize the full potential of Transformer architectures for distributed groundwater surrogate modeling, several challenges must first be addressed. Groundwater systems involve heterogeneous information sources, including dynamic state variables (e.g., pressure and evapotranspiration) and static hydrogeological attributes (e.g., topography, land surface characteristics, and subsurface hydraulic properties), which interact across multiple temporal and spatial scales. Effectively integrating these heterogeneous dynamic and static variables into a Transformer framework therefore becomes an important modeling question (Engdahl, 2025; Liesch and Ohmer, 2026). In addition, groundwater surrogate models are expected to remain reliable under different hydrogeological conditions, including shallow and deep water table regions, as well as under rare hydrological events. Similar to recent developments in foundation models, improving model robustness may require not only architectural advances but also better coverage of rare hydrological states within the training data (Chen et al., 2025).

Motivated by these challenges, this study presents an initial exploration of Transformer-based surrogate modeling for distributed groundwater simulations using a representative watershed extracted from a continental-scale ParFlow-CLM simulation over China. Specifically, we address three scientific questions. First, can a Transformer-based surrogate model accurately reproduce long-term groundwater dynamics under autoregressive prediction? Second, how should dynamic hydrological variables and static hydrogeological information be integrated within the Transformer framework, and how do their contributions vary across different groundwater conditions? Third, can physics-based data augmentation, generated by perturbing meteorological forcing and rerunning the numerical model, improve model robustness under relatively rare hydrological extremes? Rather than demonstrating that Transformers universally outperform recurrent models, our objective is to provide one of the first systematic evaluations of Transformer architectures for distributed groundwater surrogate modeling, identify their strengths and limitations under different groundwater conditions, and offer practical guidance for future AI-driven groundwater modeling.

2. Study Area and ParFlow-CLM Simulations

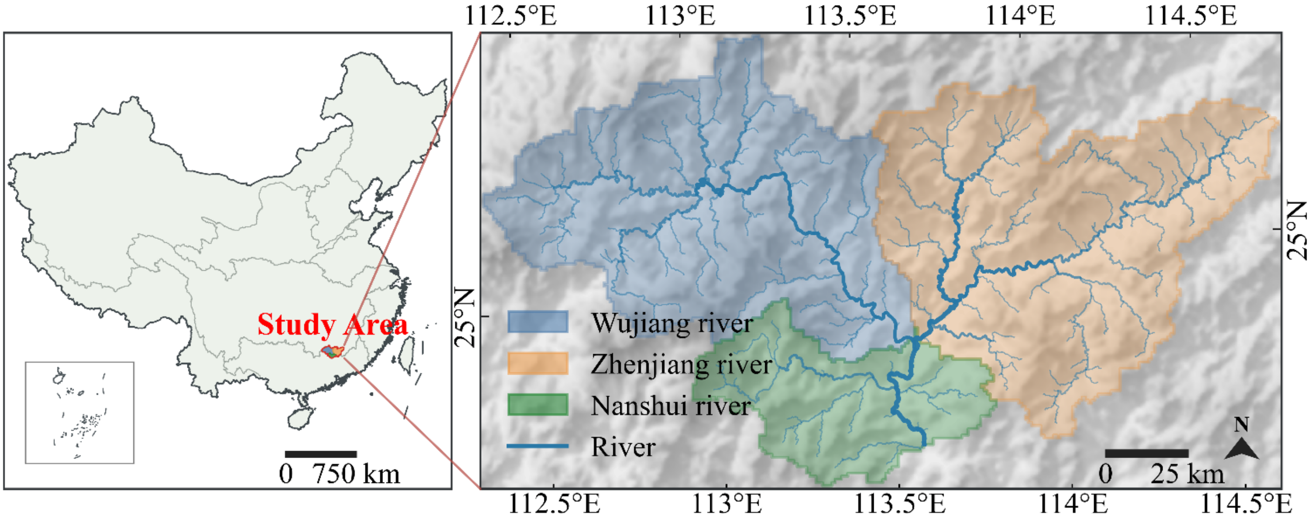

Figure 1. Study area defined by the regional ParFlow-CLM simulation domain in the upper Beijiang River basin. The domain comprises three tributary subbasins: the Wujiang, Zhenjiang, and Nanshui River subbasins. The left panel shows its location within the Pearl River basin, whereas the right panel delineates the complete domain, including the three subbasins and the associated river network.

The study area is the upper Beijiang River basin (UBRB) within the Pearl River basin in southern China, covering approximately 34,000 km² and comprising three tributary subbasins: the Wujiang, Zhenjiang, and Nanshui River subbasins (**Figure 1**). The data used in this study were obtained from an existing regional ParFlow-CLM model of UBRB (Sun et al., 2026). ParFlow is an integrated hydrologic model that represents overland flow and three-dimensional variably saturated subsurface flow (Kollet and Maxwell, 2006). During the coupling, ParFlow provides soil-moisture and pressure-head (Press.) states to CLM, whereas CLM calculates the land-surface water and energy balances and returns the resulting layer-resolved P−ET (PME) fluxes to ParFlow as source–sink forcing through the upper four coupled subsurface layers (Maxwell and Miller, 2005; Maxwell and Kollet, 2008). The regional ParFlow configuration was extracted from CONCN 1.0 (Yang et al., 2025) and retained its model structure and parameterization, whereas the transient ParFlow-CLM simulations were driven by ERA5-Land meteorological forcing (Muñoz-Sabater et al., 2021).

Detailed descriptions of CONCN 1.0 and of the construction and evaluation of the regional ParFlow-CLM model are provided by Yang et al. (2025) and Sun et al. (2026), respectively; the model characteristics and simulation data directly relevant to the present study are summarized below. The regional model has a horizontal resolution of approximately 1 km and contains 252 and 146 grid cells in the x and y directions, respectively. The subsurface is represented by 10 vertical layers with a total thickness of approximately 492 m. Hourly ParFlow-CLM simulations for WY2019–WY2021 (where WY denotes water year) were used as the reference data for surrogate-model development and evaluation. For the data-augmentation experiments, additional ParFlow-CLM simulations were conducted by multiplying the precipitation forcing by factors of 1.4 and 1.8; details of these simulations and the associated sample-selection strategies are provided in Section 4.

The dynamic model outputs included pressure head, saturation, and the layer-resolved PME fluxes. In this study, the surrogate was developed specifically for the ParFlow component as a step toward its future hybrid coupling with a land-surface model. The surrogate was trained offline using precomputed ParFlow-CLM simulation outputs, without interactive coupling to CLM: the 10-layer pressure-head fields were used as both the dynamic state input and prediction target, while the four-channel PME fields associated with the four coupled subsurface layers were supplied as prescribed dynamic forcing. The static inputs comprised 31 channels representing the van Genuchten α and n parameters (Van Genuchten, 1980), hydraulic conductivity, porosity, Manning's roughness coefficient, and surface slopes. The roles and channel numbers of these variables are summarized in **Table 1**. Saturation was retained as part of the ParFlow-CLM reference simulations but was not used as a surrogate input or prediction target. Water table depth (WTD) was diagnosed from the vertical pressure-head profiles and used for model evaluation.

Table 1. *ParFlow-CLM variables and parameters used in the groundwater surrogate model.*

Variable	Channels	Description
Pressure head	10	Groundwater pressure head used as the dynamic state input and prediction target of the surrogate model
PME	4	Layer-resolved net P−ET flux transferred from CLM to ParFlow as source–sink forcing (positive: source; negative: sink)
van Genuchten α	4	van Genuchten parameter related to inverse air-entry pressure in the soil-water retention curve
van Genuchten n	4	van Genuchten parameter controlling the shape of the soil-water retention curve
Hydraulic conductivity	10	Hydraulic conductivity in the x direction
Porosity	10	Fraction of void space in the subsurface medium
Manning's coefficient	1	Manning's roughness coefficient for overland flow
Slope x	1	Surface slope in the x direction
Slope y	1	Surface slope in the y direction

3. Groundwater-Adapted PredFormer Framework

3.1 PredFormer as the Backbone Architecture

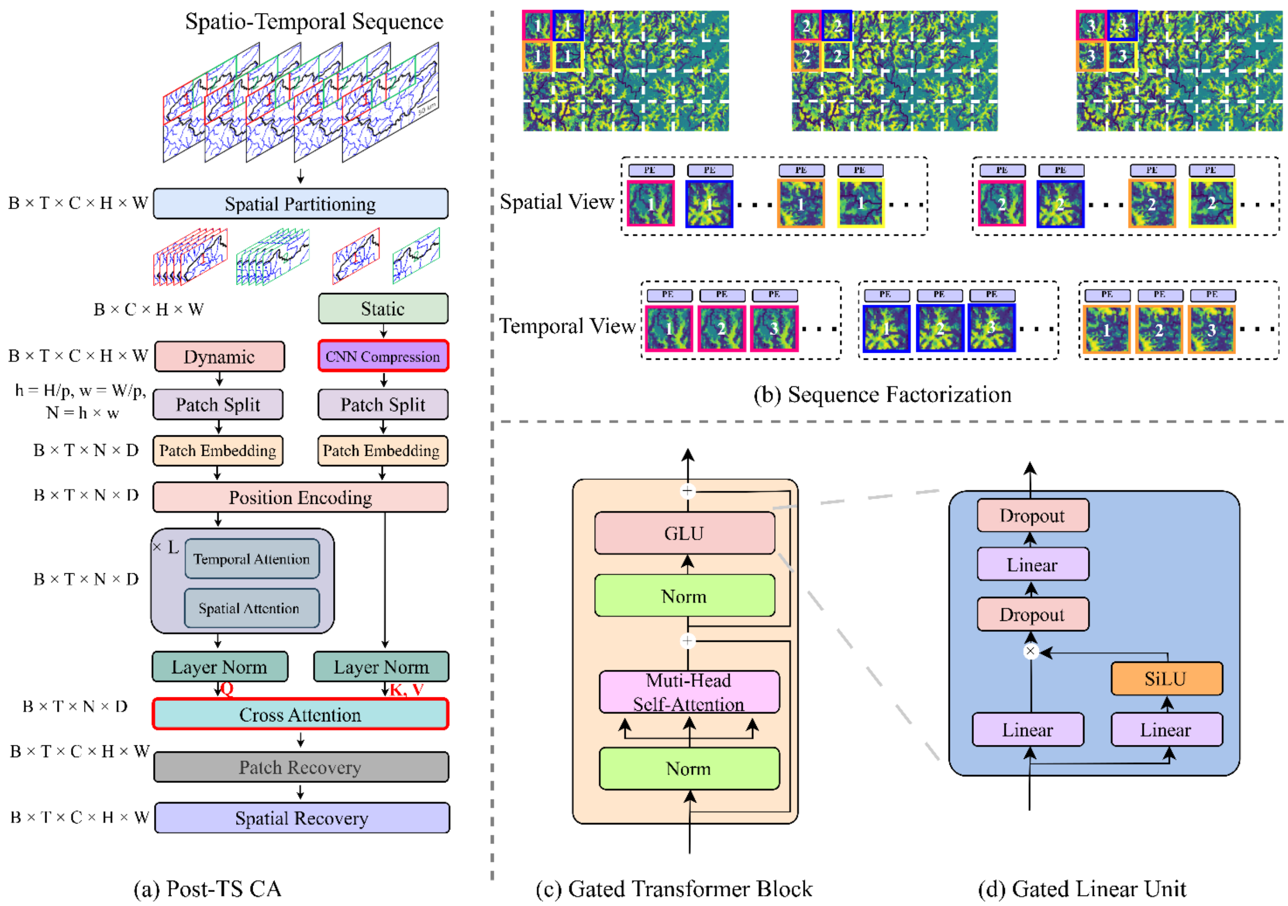

Figure 2. Groundwater-adapted PredFormer architecture. Panel (a) presents the overall framework. Dynamic pressure-head fields and prescribed PME are processed in overlapping spatial windows, divided into non-overlapping patches, and embedded as spatiotemporal tokens. Static attributes are compressed using a convolutional neural network (CNN) encoder and tokenized separately. The encoded dynamic tokens query the static tokens through post-temporal–spatial cross-attention, with dynamic tokens providing queries and static tokens providing keys and values. The model predicts pressure residuals relative to the final pressure state in the input sequence, and predictions from overlapping windows are averaged during spatial reconstruction. Panel (b) illustrates temporal-first factorized attention, panel (c) shows a Gated Transformer Block, and panel (d) shows the SwiGLU (Shazeer, 2020) operation. PE denotes positional encoding; Q, K, and V denote queries, keys, and values, respectively.

PredFormer is a pure Transformer framework developed for spatiotemporal predictive learning, that is, predicting future states from observed spatiotemporal sequences (Tang et al., 2024). Its original applications represent video frames and other gridded fields as sequences of spatial tokens and learn their evolution over time. Groundwater dynamics exhibit a comparable spatiotemporal structure: distributed multilayer pressure-head fields contain complex spatial patterns, and these spatially distributed states evolve continuously through time. This correspondence motivated the use of

PredFormer as the backbone of the ParFlow groundwater surrogate. Among the architectures evaluated in the original PredFormer study, the temporal-first factorized encoder (Fac-T-S) achieved the best performance on WeatherBench (Rasp et al., 2020), a gridded geoscience benchmark and the application most closely related to the present groundwater problem. We therefore adopted Fac-T-S as the starting configuration for modeling groundwater-state evolution.

Within each local spatial window, the pressure-head fields are divided into non-overlapping patches. Each patch is flattened and linearly projected into a token, after which spatiotemporal positional encoding is added to preserve its temporal and spatial location. The resulting token tensor has dimensions $B \times T \times N \times D$, where T and N denote the numbers of time steps and spatial patches, respectively. Temporal attention is first applied along the T tokens associated with each fixed spatial patch. The resulting representation is then rearranged, and spatial attention is applied across the N patches independently at each time step. This factorization reduces the attention complexity from $O(T^2N^2)$ for full spatiotemporal attention to $O(NT^2+TN^2)$, while retaining separate representations of temporal evolution and spatial interaction.

The factorized encoder produces a spatiotemporal pressure-head representation and forms the PredFormer backbone used in this study. The final token representation is linearly projected back to the patch dimensions through patch recovery, and the recovered patches are reassembled to reconstruct the future pressure-head fields. Groundwater-specific adaptations to this backbone, including residual prediction and blockwise autoregressive rollout as well as the incorporation of dynamic forcing and static attributes, are described in Sections 3.2 and 3.3. Domain partitioning and full-domain spatial reconstruction are described in Section 3.4. Detailed formulations of patch tokenization and positional encoding, Gated Transformer Blocks, and temporal-first factorized attention are provided in Supplementary Information **S1.1–S1.3**, respectively.

3.2 Residual Prediction and Autoregressive Rollout

Pressure head is a spatially coherent state field with strong temporal persistence: each future field largely inherits the preceding state, while hydrological forcing and subsurface water redistribution produce incremental changes. A future pressure-head field can therefore be represented as the latest available state plus its subsequent change. Accordingly, rather than directly reconstructing absolute future fields as in the original PredFormer, the adapted model predicts pressure-head residuals relative to the latest available pressure-head state.

These residual predictions were incorporated into a blockwise autoregressive rollout. Let t_{start} denote the forecast initialization time of the current prediction block, corresponding to the final time step of its input block. The predicted pressure head at the i-th future time step was reconstructed as

$$\widehat{\text{Press.}}_{t_{\text{start}}+i} = \widehat{\text{Press.}}_{t_{\text{start}}} + \Delta\widehat{\text{Press.}}_{t_{\text{start}},\, i}, \quad i = 1, \ldots, L_{\text{out}},$$

where L_{out} denotes the number of forecast time steps in each output block, $\widehat{\text{Press.}}_{t_{\text{start}}}$ denotes the latest available pressure-head field at t_{start}, i.e., the final field of the current input block, and $\Delta\widehat{\text{Press.}}_{t_{\text{start}},\, i}$ denotes the predicted pressure-head residual at the i-th future time step. All residuals within a prediction block were defined relative to the same initial state and were not accumulated sequentially. Residual reconstruction was performed in normalized pressure space, after which the predicted pressure-head fields were transformed back to their original scale.

Both the input and output blocks consequently contained 12 hourly pressure-head fields. Each independent 720 h rollout was initialized once using a 12 h block of ParFlow-CLM reference pressure-head fields. This initial block was used to predict the first 12 h block, after which each predicted block was fed back as the input for the next prediction, without reintroducing reference pressure-head states for correction. Repeating this procedure for 60 consecutive prediction blocks produced a continuous 720 h trajectory. During model development, we also tested a 24 h input–output configuration. Because the 12 h setting yielded better predictive performance, it was adopted in this study.

3.3 Dynamic–Static Inputs and Fusion Strategies

Groundwater dynamics depend on the antecedent states of the groundwater system, temporally varying external forcing, and spatially heterogeneous hydrogeological and hydrogeomorphic conditions. The antecedent pressure-head sequence represents the prior evolution of the groundwater system, whereas PME provides dynamic source–sink forcing. Meanwhile, static attributes characterize the spatially varying subsurface and land-surface conditions that regulate the storage and transmission of water across the domain. For example, hydraulic conductivity affects subsurface water transmission, porosity influences water storage, and surface slopes define the topographic gradients driving overland flow, whereas Manning's roughness controls resistance to that flow. Therefore, dynamic forcing and static attributes may provide useful predictive information beyond antecedent pressure-head states.

We first investigated which types of information should be incorporated into the PredFormer backbone. Starting from a baseline using only pressure head (Press.), dynamic forcing and static attributes were progressively introduced, resulting in four input combinations: Press., Press. + PME, Press. + Static, and Press. + PME + Static. This experimental design was used to examine whether PME, static attributes, or their joint inclusion provided additional predictive information beyond the antecedent pressure-head sequence. To further examine the four input combinations across groundwater depths, the analysis was stratified by WTD into three zones: shallow (0–2 m), intermediate (2–20 m), and deep (>20 m).

We then considered how these additional inputs should be incorporated. Because the four-channel PME fields vary over time and are temporally aligned with the 10-channel pressure-head fields, they were directly concatenated with the pressure-head fields along the channel dimension before patch tokenization. The incorporation of static attributes required a more specific fusion design. The 31 static channels describe heterogeneous hydrogeological and hydrogeomorphic conditions and may exhibit cross-channel redundancy. For example, hydrogeological properties may covary spatially with slope-related hydrogeomorphic information. We therefore compared four strategies for integrating static attributes into the dynamic representation.

The first strategy, Raw-Static Concatenation, repeated the original 31-channel static fields along the temporal dimension and directly concatenated them with the dynamic inputs before patch tokenization. The second strategy, CNN-Compressed Static Concatenation, first compressed the 31 static channels into eight feature channels using a CNN encoder with a 3 × 3 convolutional kernel and then repeated and concatenated the compressed features with the dynamic inputs (Alzubaidi et al., 2021). In addition to these concatenation-based strategies, we further considered cross-attention to integrate the static information into the evolving dynamic representation. Because this operation can be introduced at different stages of the PredFormer backbone, two configurations were evaluated. Pre-temporal–spatial (Pre-TS) Cross-Attention applied cross-attention before temporal-first factorized attention, whereas Post-temporal–spatial (Post-TS) Cross-Attention applied it after temporal and spatial attention and before patch recovery and pressure prediction.

For cross-attention, let Z_d denote the dynamic-token representation at the selected fusion location and Z_s denote the CNN-compressed static-token representation. The fusion operation was formulated as

$$Q = \mathrm{LN}(Z_\mathrm{d}), \quad K = V = \mathrm{LN}(Z_\mathrm{s}),$$

$$Z_\mathrm{f} = Z_\mathrm{d} + \mathrm{CrossAttn}(Q, K, V),$$

where LN denotes layer normalization and Z_f denotes the fused representation. In the cross-attention operation, the normalized dynamic tokens serve as queries, whereas the normalized static tokens provide the keys and values. The query associated with each dynamic token is compared with the static keys to determine the attention weights assigned to different static tokens. The corresponding static values are then weighted and aggregated to produce a static-information update for that dynamic token. Because the cross-attention output retains the token organization and feature dimension of Z_d, it can be added back to the original dynamic representation through a residual connection. In this way, the evolving dynamic representation is conditioned on the local static attributes while preserving the information already encoded in the dynamic tokens.

For the input-combination experiments, Post-TS Cross-Attention was used whenever static attributes were included. For the fusion-strategy experiments, all four strategies were evaluated using the complete Press. + PME + Static input combination. In both the Pre-TS and Post-TS Cross-Attention configurations, the 31-channel static attributes were first compressed into eight feature channels using the same CNN encoder.

3.4 Model Implementation and Evaluation

Training samples were constructed through combined spatial and temporal sampling. Spatially, an additional windowing step was introduced before patch tokenization to adapt the PredFormer backbone to the full regional domain. The 252 × 146 grid was divided into overlapping spatial windows of 80 × 64 grid cells, with horizontal and vertical strides of 40 and 32 cells, respectively. Each window was further divided into non-overlapping 8 × 8 patches, yielding a 10 × 8 grid of patches, or 80 spatial tokens, at each time step. Because adjacent windows overlapped, shared grid cells were represented using spatial context from more than one window. Window-level predictions were subsequently mapped back to the complete domain, and predictions for grid cells covered by multiple windows were reconstructed by arithmetic averaging. Temporally, samples were extracted using a stride of 6 h. For each spatial window, a sample contained 12 consecutive hourly pressure-head fields and a 12 h sequence of prescribed PME fields as dynamic inputs and was used to predict the subsequent 12 h pressure-head block. At each sequence position, the pressure-head state at time *t* was paired with the prescribed PME forcing at time *t*+1, which was used to advance the system from *t* to *t*+1. For each sample, the static attributes were extracted from the same spatial window as the dynamic inputs and remained unchanged over time.

The ParFlow-CLM simulations from WY2019–WY2020 were used for model training, and the WY2021 simulation was used for testing. The test period was divided into 12 consecutive, non-overlapping segments of 720 h, corresponding to a 30-day forecast horizon. Each segment was initialized and evaluated independently, and prediction errors were not propagated across segment boundaries. All input and target variables were standardized before training. The mean and standard deviation used for standardization were calculated from the WY2019–WY2020 training data and applied to all training and test samples. Variables containing multiple vertical layers were standardized independently for each layer. The model was trained by minimizing the unweighted mean squared error between the predicted and ParFlow-CLM reference pressure-head fields in standardized space, averaged over all predicted elements in each training batch. All models were trained for 60 epochs using the AdamW optimizer with a batch size of 28 and an initial learning rate of 3×10^{-4}. A cosine learning-rate schedule was applied throughout training. The checkpoint from the final training epoch was used to generate all test-set predictions.

WTD was calculated from both the predicted and ParFlow-CLM reference pressure-head fields. For segment *i*, forecast hour *t*, and grid cell *k*, the absolute WTD error was defined as

$$e_{i,t,k} = |\widehat{WTD}_{i,t,k} - WTD_{i,t,k}|.$$

Here, the hatted WTD term denotes the predicted value, and the unhatted WTD term denotes the ParFlow-CLM reference value. The spatial mean absolute WTD error, $E_{i,t}$, was obtained by averaging $e_{i,t,k}$ over all grid cells at each forecast hour:

$$E_{i,t} = \frac{1}{N_g}\sum_{k=1}^{N_g} e_{i,t,k},$$

where N_g is the number of grid cells. Let N_s and T denote the number of test segments and the number of forecast hours per segment, respectively ($N_s = 12$ and $T = 720$). The mean error at forecast hour t across all test segments, E_t, was calculated as

$$E_t = \frac{1}{N_s}\sum_{i=1}^{N_s} E_{i,t}.$$

The mean error over all forecast hours within segment i, E_i, was defined as

$$E_i = \frac{1}{T}\sum_{t=1}^{T} E_{i,t}.$$

The overall mean error across all segments and forecast hours, E, was therefore calculated as

$$E = \frac{1}{N_s}\sum_{i=1}^{N_s} E_i = \frac{1}{T}\sum_{t=1}^{T} E_t.$$

The hourly change in spatial mean absolute WTD error was calculated as

$$\Delta E_{i,t} = E_{i,t} - E_{i,t-1}.$$

A positive value indicates an increase in spatial mean absolute WTD error between two consecutive forecast hours.

3.5 PredRNN as the Recurrent Reference Model

Recurrent architectures have been widely used for groundwater surrogate modeling because their hidden states allow temporal information to be propagated as pressure-head fields evolve. PredRNN was selected as the recurrent reference because its convolutional spatiotemporal memory jointly represents temporal and spatial dependencies while preserving the gridded structure of distributed pressure-head fields (Wang et al., 2017; Bennett et al., 2024; Yang et al., 2026a). Whereas PredFormer generated a 12 h pressure-head block in a single forward pass, PredRNN advanced the pressure-head field sequentially at hourly intervals. The implemented PredRNN and PredFormer contained 76,784 and 9.04 million trainable parameters, respectively.

PredRNN used the same forecast origins, target pressure-head fields, prescribed PME fields, and static attributes as PredFormer. During training, the ParFlow-CLM pressure-head field immediately preceding each 12 h target sequence served as the initial input. At each target hour, PredRNN predicted a residual relative to the preceding pressure-head field and added this residual to reconstruct the absolute pressure-head field. The reconstructed field was subsequently fed back as the pressure input for the next recurrent update. The corresponding PME field and CNN-encoded static attributes were supplied at each hourly step. The training loss was calculated from the reconstructed pressure-head fields and averaged over the 12 target hours.

For the 720 h evaluation, PredFormer was initialized with a 12 h sequence of reference pressure-head fields, whereas PredRNN was initialized with the final pressure-head field from the same reference period. This ensured that the two models shared the same first forecast hour and the same 720 h evaluation period. Thereafter, predicted pressure-head fields were recursively fed back according to the respective rollout schemes, without reference-state correction. PME remained prescribed, and the static attributes remained fixed throughout each rollout.

4. Precipitation Regimes and Data Augmentation

Extreme dry and wet conditions are often underrepresented in finite training records, which may limit a surrogate model's predictive ability when analogous conditions are encountered in prediction (Leonarduzzi et al., 2022; Xu et al., 2025). Physics-based simulations provide a practical means of generating additional, physically consistent examples beyond those contained in the unperturbed record. We therefore examined whether precipitation-regime-specific data augmentation, in which training samples representing selected precipitation conditions were added, could improve long-horizon groundwater prediction under the corresponding precipitation regimes.

Rather than directly perturbing pressure head or PME, which could disrupt the coupled relationships among precipitation forcing, water exchange between the land surface and subsurface, and groundwater states, we generated additional simulations by modifying the precipitation component of the ERA5-Land forcing. For each of the two training years, WY2020 and WY2021, the precipitation forcing was multiplied by factors of 1.4 and 1.8, while all other meteorological forcings remained unchanged. ParFlow-CLM was then rerun for both perturbation scenarios, producing four additional simulation years in which pressure head, PME, saturation, and WTD remained physically consistent with the modified precipitation forcing.

Precipitation regimes were defined using the 24 h domain-mean accumulated precipitation, denoted as P_{24}. Each 24 h window was classified as Dry ($P_{24} < 1$ mm), Light ($1 \leq P_{24} < 10$ mm), Moderate ($10 \leq P_{24} < 25$ mm), or Heavy ($P_{24} \geq 25$ mm). Two windowing schemes were used for different purposes. Consecutive non-overlapping 24 h windows were used first to characterize hourly WTD responses in the unperturbed WY2019–WY2021 simulations and later to analyze WTD prediction errors, $\Delta E_{i,t}$, in the unperturbed WY2019 test simulation by precipitation regime. In contrast, overlapping 24 h windows with a temporal stride of 6 h were used to construct the surrogate-training samples and assign them to precipitation regimes for data augmentation. The same precipitation thresholds were applied to both windowing schemes.

Among the three unperturbed simulation years, WY2019 had the highest annual precipitation, with 1933.0 mm compared with 1509.3 mm in WY2020 and 1144.6 mm in WY2021. The unperturbed WY2019 simulation was therefore held out as the test period, whereas the unperturbed WY2020–WY2021 simulations formed the baseline training set. Additional training samples were drawn only from the precipitation-perturbed WY2020–WY2021 simulations; no samples from WY2019 were used for model training.

Four augmentation strategies were compared with the baseline training set (**Table 2**). All-1.4× added all 2916 candidate samples from the 1.4× precipitation simulations for WY2020–WY2021. Dry-1000 added 1000 Dry samples, ModHeavy-1000 added 1000 samples comprising 687 Moderate and 313 Heavy samples, and Heavy-all added all 313 available Heavy samples. For the Dry-1000, ModHeavy-1000, and Heavy-all strategies, samples were selected from the combined set of candidate samples generated by the 1.4× and 1.8× precipitation simulations for WY2020–WY2021. All configurations were evaluated using the same unperturbed WY2019 test period to determine whether augmenting selected precipitation regimes improved prediction under the corresponding precipitation conditions.

Table 2. Precipitation-regime composition of the additional training samples used in each augmentation strategy.

Strategy	Added samples				
	Total	Dry	Light	Moderate	Heavy
All-1.4×	2916	1311	1101	390	114
Dry-1000	1000	1000	0	0	0
ModHeavy-1000	1000	0	0	687	313
Heavy-all	313	0	0	0	313

5. Results and Discussion

5.1 Long-Horizon Groundwater Prediction and Error Evolution

Computational efficiency was evaluated using wall-clock runtime for a one-year simulation over the same regional domain. ParFlow-CLM was executed using 24 CPU cores on an AMD EPYC 9654 96-Core Processor, whereas PredFormer inference was performed using an NVIDIA A100-SXM4-80GB GPU. Under these computational configurations, PredFormer required approximately 220 s, compared with about 2.5 h for ParFlow-CLM, corresponding to an approximately 41-fold speedup. The reported PredFormer runtime included data loading, preprocessing, and spatial reconstruction. To characterize long-horizon error propagation, **Figure 3** presents the spatial median of the absolute WTD error (referred to as the median error within this section) together with the spatial q25–q75 and q10–q90 ranges for all 12 test segments. A 720 h, or 30-day, horizon represents a practical timescale for examining groundwater evolution during prolonged wet and dry conditions relevant to drought and flood preparedness. Across the 12 segments, the median, q75, and q90 errors were initially small and generally increased with lead time. At 720 h, the final median error ranged from 0.071 to 0.140 m across segments.

Across the 12 segments, two distinct aspects of error evolution were evident. First, the smoothness of the WTD error trajectories was generally associated with the temporal variability of precipitation (σ_P). Segments with relatively low σ_P, such as Segments 1–4, exhibited comparatively smooth and gradual error accumulation, whereas segments with more variable precipitation, including Segments 5–12, generally showed more pronounced fluctuations in their error trajectories. However, none of the final-hour median, q75, or q90 errors showed a clear monotonic relationship with either μ_P or σ_P (**Table 3**). Second, the most pronounced changes in error frequently coincided with abrupt transitions between relatively dry and wet conditions. In Segment 11, for example, the onset of substantial precipitation near hour 7380 was accompanied by a sharp error increase, whereas the subsequent period of sustained precipitation produced a comparatively gradual increase. More strikingly, in Segment 9, the error remained relatively low during the initially wet period but increased markedly as precipitation weakened and conditions became drier. Similar event-associated error fluctuations were also visible in several other segments.

The segment-level correlation analysis further showed that the 720 h mean of the median error was only weakly associated with precipitation statistics (**Table 3**). Their strongest and most consistent relationships were observed for the 720 h mean of q90 error, with Spearman correlations of 0.629 for μ_P and 0.608 for σ_P. Thus, precipitation amount and temporal variability were associated primarily with the upper tail of the spatial error distribution rather than with a uniform increase in domain-wide or final-hour error. Together with the event-scale trajectories, these results suggest that larger grid-cell errors were more closely associated with segment-scale precipitation statistics, whereas fluctuations in the error trajectories coincided more closely with abrupt wet-dry transitions.

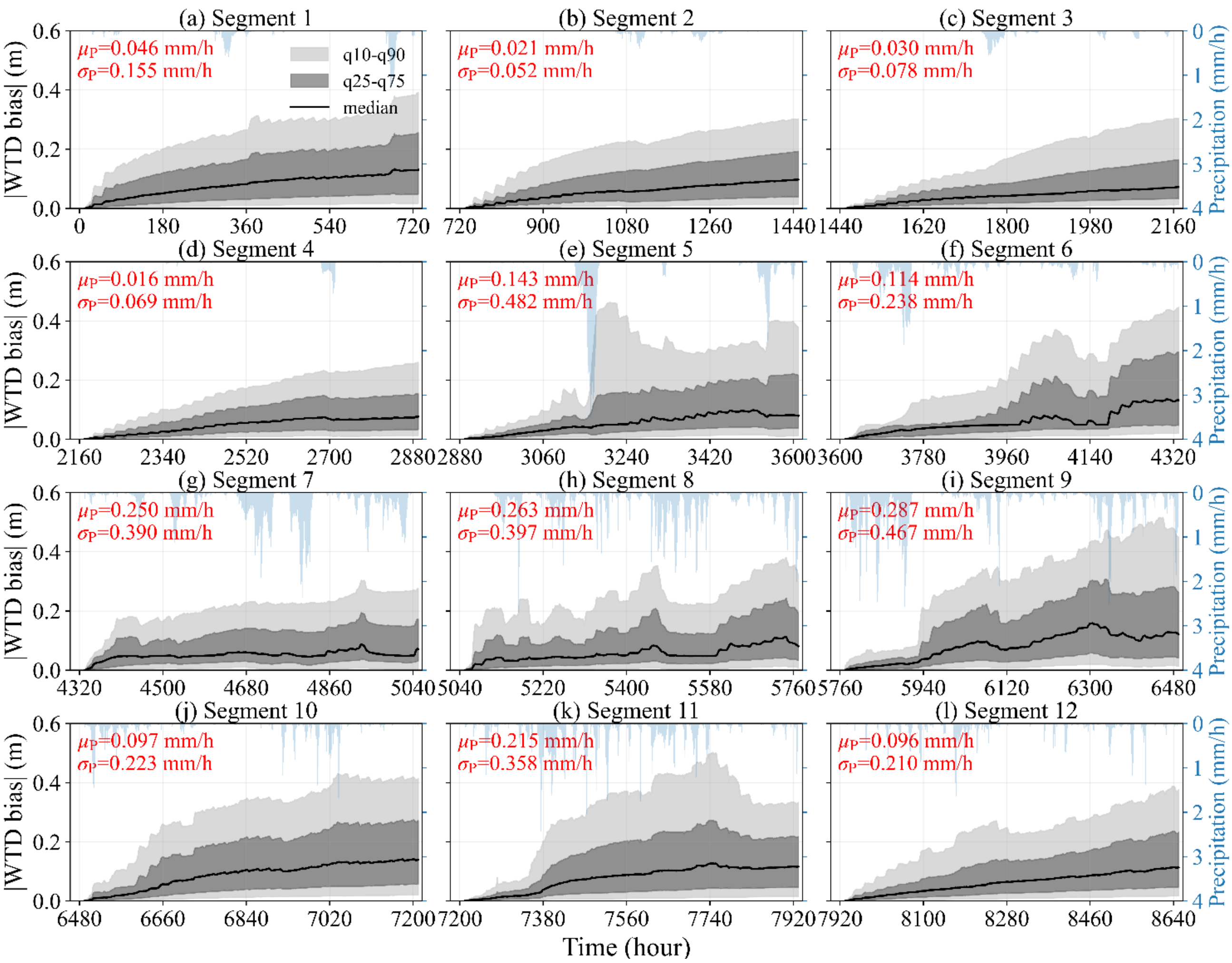

Figure 3. Segment-wise evolution of precipitation and WTD prediction error during 720 h autoregressive prediction. Panels (a–l) show the 12 independently initialized, non-overlapping 720 h segments from the independent WY2021 test simulation. Black curves show the spatial median of the absolute WTD error, dark and light shaded bands show the spatial q25–q75 and q10–q90 ranges, respectively, and blue bars show domain-mean hourly precipitation on the secondary *y*-axis. Red annotations report the mean (μ_P) and standard deviation (σ_P) of domain-mean hourly precipitation within each segment.

Table 3. Segment-level correlations between precipitation statistics and WTD prediction-error metrics (n = 12).

Precipitation metric	WTD error metric	Pearson r	Spearman ρ
Precipitation mean (μ_P)	720 h mean of spatial mean	0.462	0.476
	720 h mean of spatial median	0.247	0.287
	720 h mean of spatial q75	0.465	0.566
	720 h mean of spatial q90	**0.554**	**0.629**
	final-hour spatial mean	0.114	0.238
	final-hour spatial median	-0.023	0.105
	final-hour spatial q75	0.135	0.287
	final-hour spatial q90	0.192	0.378
Precipitation standard deviation (σ_P)	720 h mean of spatial mean	0.494	0.469
	720 h mean of spatial median	0.246	0.175
	720 h mean of spatial q75	0.467	0.469
	720 h mean of spatial q90	**0.600**	**0.608**
	final-hour spatial mean	0.203	0.231
	final-hour spatial median	-0.02	0.035
	final-hour spatial q75	0.233	0.259
	final-hour spatial q90	0.328	0.385

Figure 4 further illustrates the spatial evolution of WTD prediction during a representative segment (Segment 4). The adapted PredFormer reproduced the dominant spatial organization of the ParFlow-CLM reference WTD field and retained its broad spatial pattern as the rollout progressed. The signed differences were small at the beginning of the forecast but became progressively larger and more spatially heterogeneous with increasing lead time. Positive and negative differences were interspersed at relatively fine spatial scales, indicating that the prediction error did not develop as a spatially uniform offset. By 720 h, positive differences were more prevalent in the northwestern part of the domain, whereas negative differences were more prominent toward the southeast, revealing a broad spatial organization superimposed on the finer-scale error pattern. A complementary analysis across all 12 segments (**Table 4**) further stratified the absolute WTD errors according to the reference WTD. For the Press. + PME + Static configuration, the mean absolute errors, E, were 0.08913 m in the shallow zone (0–2 m), 0.02569 m in the intermediate zone (2–20 m), and 0.05682 m in the deep zone (>20 m). Thus, the errors were largest in shallow-groundwater areas, smallest at intermediate depths, and moderate in deep-groundwater areas.

The adapted PredFormer provides a representation aligned with the spatiotemporal characteristics of distributed groundwater fields. Temporal-first attention relates successive pressure-state representations, spatial attention captures dependencies among spatial patches at each time step, and residual prediction expresses each output block as a change from the latest pressure state. Together, the results support the feasibility of the adapted PredFormer for long-horizon groundwater emulation, while also showing that its prediction errors remain sensitive to abrupt transitions between wet and dry conditions. This remaining sensitivity highlights the importance of adequately representing such hydrological transitions in the training data.

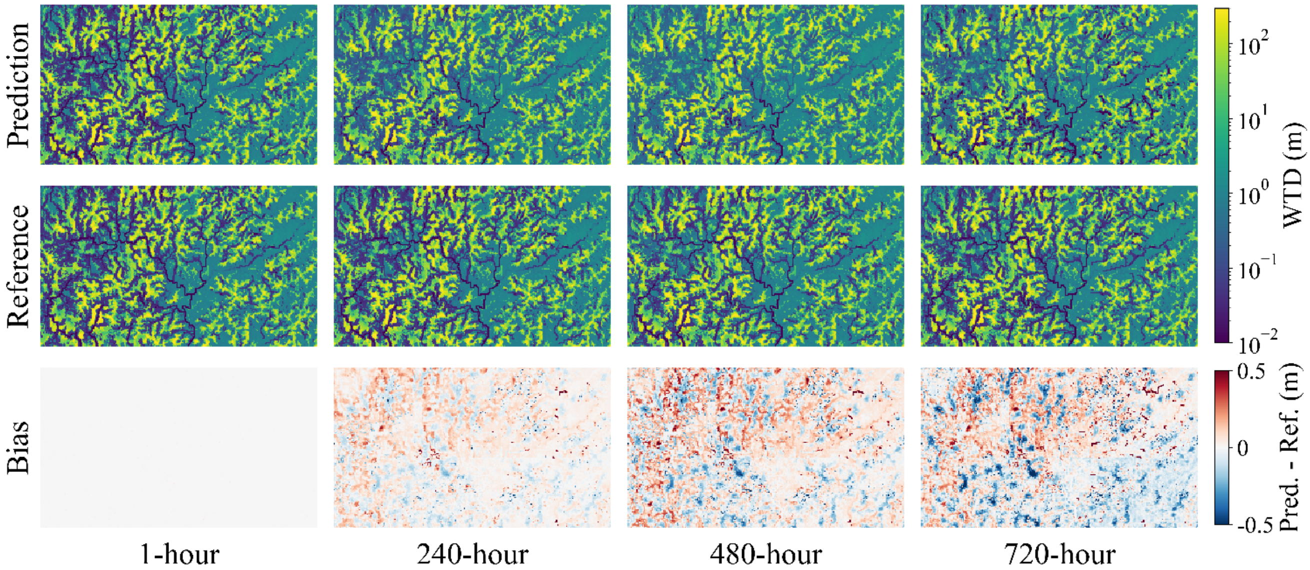

Figure 4. Spatial distributions of predicted and reference WTD and their differences at selected lead times during Segment 4. Segment 4 is taken from the independent WY2021 test simulation and spans hours 2172–2891. Columns show lead times of 1, 240, 480, and 720 h, corresponding to hours 2172, 2411, 2651, and 2891 of the WY2021 simulation, respectively. The first and second rows show the PredFormer predictions and corresponding ParFlow-CLM references, respectively. The bottom row shows the signed WTD prediction error, calculated as prediction minus reference. The first column represents the first predicted hour rather than the initialized state.

5.2 Effects of Input Composition and Static-Attribute Fusion Strategies

The segment-wise results showed a broadly consistent pattern among the four input combinations (**Figure S2**). Adding static attributes to pressure head alone generally maintained or reduced the WTD error, although performance deteriorated in several segments, including Segments 6–9. Adding PME to pressure head produced a more consistent improvement, reducing the error across all 12 segments. In contrast, adding static attributes after PME had already been included did not provide a systematic additional benefit: the Press. + PME + Static configuration was comparable to or slightly worse than Press. + PME in most segments, although exceptions occurred, such as Segment 3, where the full input combination performed best. The across-segment mean error trajectory, E_t, summarized these patterns (**Figure 5a**): the overall mean error, E, decreased from 0.151 m for Press. alone to 0.138 m with static attributes and to 0.099 m with PME, while the full Press. + PME + Static configuration produced the same mean error of 0.099 m. Segment 11 provided a particularly clear example (**Figure 5b**), with segment-mean errors, E_i, of 0.301, 0.248, 0.117, and 0.125 m for Press., Press. + Static, Press. + PME, and Press. + PME + Static, respectively. These results indicate that PME provided the dominant and most consistent additional information, whereas the contribution of static attributes was smaller and depended on whether dynamic forcing had already been included.

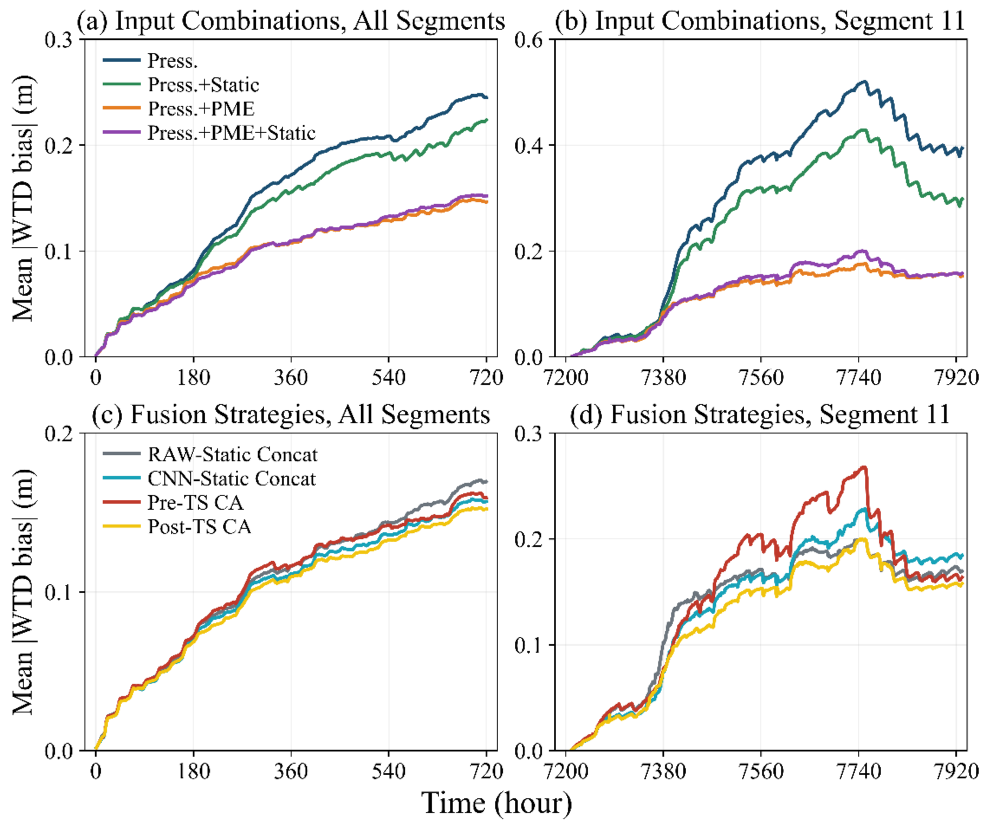

Figure 5. Effects of input composition and static-attribute fusion strategies on 720 h autoregressive WTD prediction in the independent WY2021 test simulation. Panel (a) shows the spatial-mean absolute WTD error averaged across the 12 segments for the four input combinations. Panel (c) shows the corresponding comparison among the four static-attribute fusion strategies. Panels (b) and (d) show the input-combination and fusion-strategy results, respectively, for Segment 11.

The effects of the additional inputs varied systematically among the three WTD regimes (**Table 4**). In the shallow zone (0–2 m), adding PME to pressure head produced the largest improvement, reducing the overall mean error within this zone from 0.16472 to 0.07754 m, or by 52.93%. Adding static attributes alone produced a smaller reduction of 14.09%, while combining PME and static attributes resulted in an error of 0.08913 m. In the intermediate zone (2–20 m), static attributes provided the greatest improvement, reducing the error from 0.02395 to 0.02185 m, or by 8.77%, whereas the configurations containing PME produced slightly larger errors than Press. alone. In the deep zone (>20 m), Press. alone achieved the lowest error of 0.05623 m, and none of the additional-input configurations provided further improvement. These results reveal a depth-dependent shift in the information most useful for groundwater prediction: dynamic PME forcing was most informative for shallow groundwater, static attributes were more useful at intermediate depths, and the antecedent pressure-head state alone was sufficient for the deepest groundwater.

This depth dependence is consistent with the changing connection between groundwater and land-surface forcing. Shallow water tables respond relatively directly to the upper-layer source–sink exchange represented by PME, making explicit information about the time-varying forcing particularly valuable. At intermediate depths, the surface-derived signal must propagate through a thicker unsaturated zone and is therefore attenuated and temporally smoothed. The magnitude and timing of the transmitted response become increasingly dependent on static hydraulic properties that regulate infiltration, storage, and vertical redistribution, helping explain the greater benefit of static attributes in this zone. For WTD greater than 20 m, the direct influence of land-surface forcing over the evaluated 720 h horizon is likely weaker, and groundwater evolution may be governed more strongly by antecedent subsurface conditions and slower lateral or regional groundwater flow. Because the pressure-head sequence already contains the integrated effects of these prior conditions, adding PME or static attributes supplied little additional predictive information in the deep zone.

Table 4. Mean absolute WTD error averaged across all test segments and forecast hours for each WTD regime and input combination. Percentages in parentheses indicate changes relative to the pressure-head-only configuration within each regime.

WTD regimes	Mean absolute WTD errors (m)			
	Press.	**Press. + PME**	**Press. + Static**	**Press. + PME + Static**
Shallow (0–2 m)	0.16472	0.07754 (-52.93%)	0.14151 (-14.09%)	0.08913 (-45.89%)
Intermediate (2–20 m)	0.02395	0.02500 (+4.38%)	0.02185 (-8.77%)	0.02569 (+7.27%)
Deep (>20 m)	0.05623	0.05954 (+5.89%)	0.05936 (+5.57%)	0.05682 (+1.05%)

Compared with the choice of input variables, the static-fusion strategy produced relatively small differences in WTD prediction error (**Figure S3**). The four configurations showed broadly similar error trajectories across most segments, although their relative rankings varied from one segment to another. Some fusion configurations even slightly increased the error in particular segments. Nevertheless, Post-TS Cross-Attention showed the most consistent, although modest, advantage. Averaged across the 12 segments, the overall WTD errors, E, were 0.107 m for Raw-Static Concatenation, 0.102 m for CNN-Compressed Static Concatenation, 0.106 m for Pre-TS Cross-Attention, and 0.099 m for Post-TS Cross-Attention (**Figure 5c**). Thus, CNN compression alone produced a modest improvement over direct concatenation, and applying cross-attention after temporal–spatial encoding provided a further reduction in error. In contrast, introducing cross-attention before temporal–spatial encoding largely removed the benefit obtained through CNN compression. At a lead time of 720 h, Post-TS Cross-Attention reduced the error by 10.2% relative to Raw-Static Concatenation (**Figure 5c**) and achieved the lowest mean error, E_i, in seven of the 12 segments (**Figure S3**). The distinction was particularly clear in Segment 11, where Post-TS Cross-Attention performed best and Pre-TS Cross-Attention produced the largest error (**Figure 5d**).

The modest improvement obtained through CNN compression suggests that the 31 static channels contained partly redundant or spatially covarying information and could be represented more effectively by a compact set of learned features. The additional advantage of Post-TS Cross-Attention may reflect a more effective separation between dynamic-state encoding and static conditioning. Post-TS Cross-Attention therefore first resolves temporal evolution and spatial interactions from the pressure-head and PME inputs and subsequently uses the compressed static attributes to condition the encoded dynamic representation before pressure reconstruction. By contrast, introducing static information before these temporal–spatial relationships have been resolved may partly duplicate information already embedded in the antecedent pressure state and thereby interfere with the encoding of subsequent dynamic evolution.

This difference provides a plausible explanation for why Post-TS Cross-Attention produced a small but more consistent improvement, whereas Pre-TS Cross-Attention did not outperform CNN compression alone.

5.3 Comparison with a Recurrent Reference Model

Figure 6 shows that PredFormer and PredRNN exhibited distinct lead-time-dependent error behavior over the 720 h prediction horizon. PredRNN produced lower mean absolute WTD errors, E_t, during the early prediction period (**Figure 6a**), whereas PredFormer became more accurate after approximately 160 h, with the difference increasing at longer lead times. At 720 h, the across-segment mean absolute WTD error, $E_{t=720}$, was 0.152 m for PredFormer and 0.232 m for PredRNN. Averaged across all segments and lead times, the corresponding errors, E, were 0.099 and 0.136 m, respectively, and PredFormer achieved a lower segment-mean error, E_i, in 11 of the 12 test segments (**Figure S4**). Thus, the relative advantage of PredFormer emerged primarily over longer prediction horizons rather than during the initial prediction period. In addition to its lower long-horizon error, PredFormer exhibited a smoother error trajectory. This contrast was particularly evident in the precipitation-active Segment 9 (**Figure 6b**), where the PredRNN error showed pronounced temporal fluctuations, whereas the PredFormer error remained comparatively smooth. After calculating the temporal standard deviation of the spatial-mean absolute WTD error within each segment, the values averaged across the 12 segments were 0.082 m for PredRNN and 0.047 m for PredFormer, indicating that PredFormer produced less temporally variable error trajectories.

The contrasting error behavior may reflect differences in how the two models represent spatiotemporal dependencies and how frequently their predictions are fed back during autoregressive rollout. PredRNN updates the pressure field sequentially at hourly intervals. Temporally, information is carried forward through recurrent states one hour at a time, whereas spatially, its convolutional operations exchange spatial information primarily within local neighborhoods. Long-range temporal dependencies must therefore be transmitted progressively through recurrent states, while long-range spatial interactions require stacked convolutional operations or repeated updates. Consequently, rapid changes in forcing are assimilated sequentially, while prediction errors can enter the recurrent memory at each hourly update and be repeatedly propagated, potentially producing larger fluctuations and error accumulation. PredFormer instead uses temporal attention across all input times for each spatial patch and spatial attention across all patches within a window, providing more direct pathways for representing long-range spatiotemporal dependencies. Moreover, its 12 h residual predictions are generated jointly relative to the final pressure state of the input block, so predicted states are fed back only once per 12 h block rather than at every hourly step. These differences provide a plausible explanation for the smoother error trajectories and greater long-horizon accuracy of PredFormer under the tested setting.

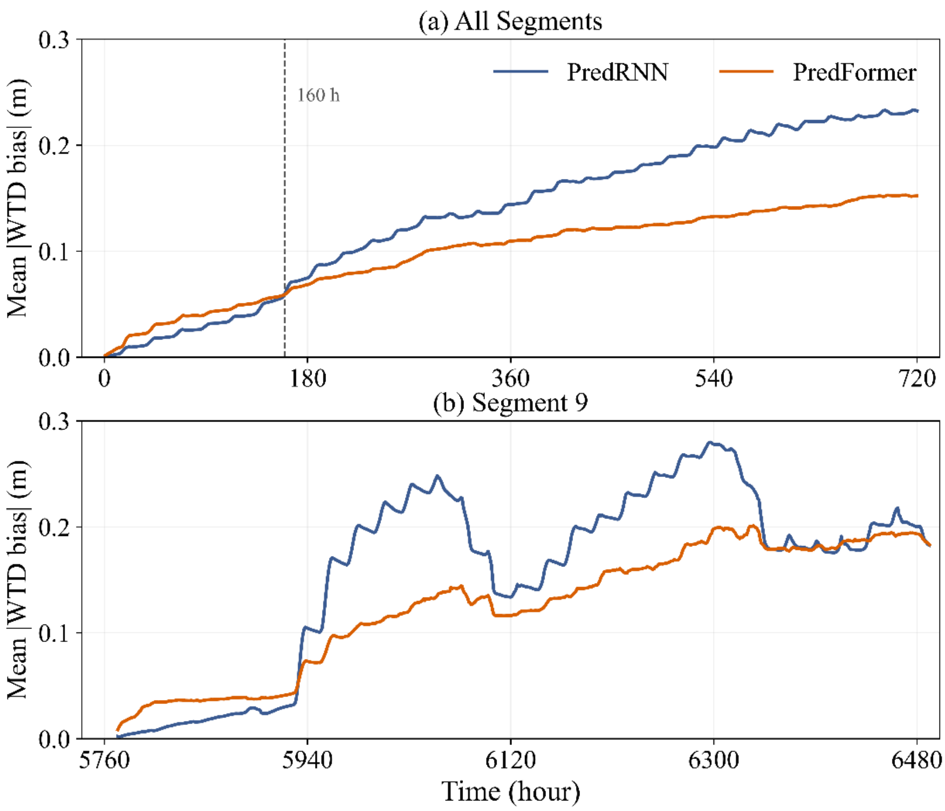

Figure 6. Long-horizon comparison between PredFormer and PredRNN. Panel (a) shows the spatial-mean absolute WTD error averaged across the 12 test segments. The dashed vertical line marks the approximate lead time at which the relative error ranking changes. Panel (b) shows the corresponding comparison for Segment 9.

5.4 Effects of Precipitation-Regime Data Augmentation

The reference simulations showed that stronger precipitation regimes were associated with larger and more variable hourly WTD responses (**Figure S5**). As the precipitation regime increased from Dry to Heavy, the distribution of ΔWTD shifted toward more negative values and became wider. Because WTD is defined as depth below the land surface, negative ΔWTD indicates a rising water table. The greater variability under stronger precipitation regimes suggests a more demanding prediction problem and motivated the precipitation-regime-specific data-augmentation experiments. The augmentation strategies produced different long-horizon error trajectories across the 12 segments (**Figure S6**). Averaged over all lead times and segments (**Figures 7a**), All-1.4× produced the lowest overall mean error, *E*, decreasing it slightly from 0.111 m for the baseline to 0.108 m. Heavy-all produced a comparable overall error, whereas Dry-1000 and ModHeavy-1000 performed less well when averaged across all precipitation conditions. These relatively small differences in the overall averages, however, concealed much stronger regime-dependent responses.

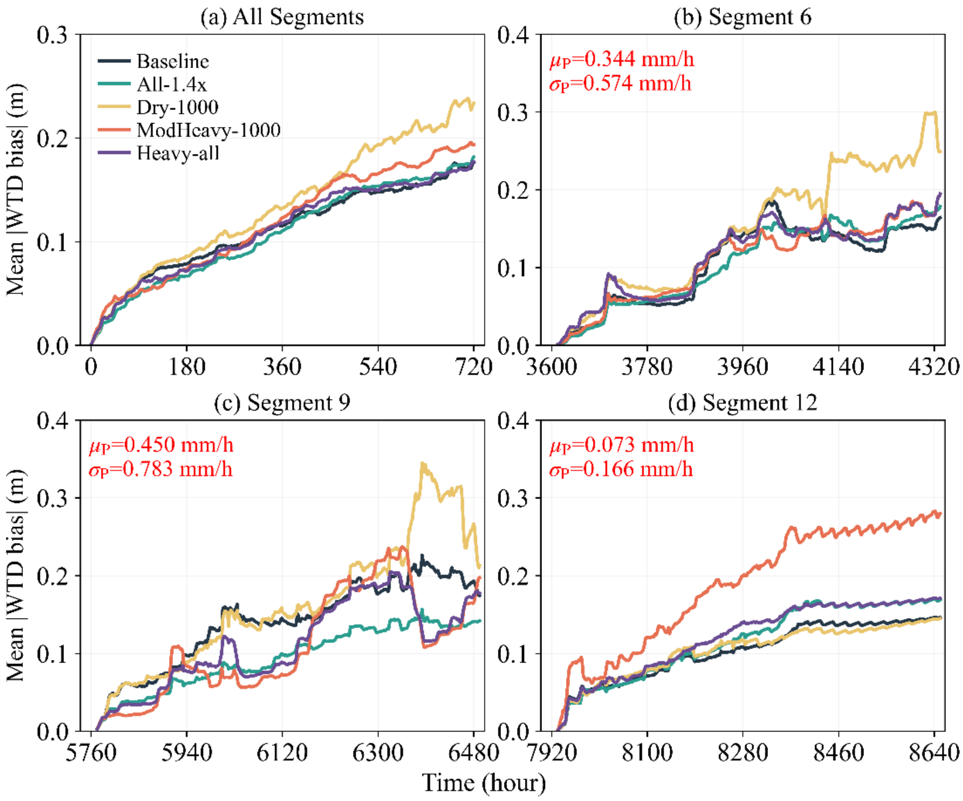

Figure 7. Effects of precipitation-regime data augmentation on 720 h autoregressive WTD prediction in the independent WY2019 test simulation. Panel (a) shows the spatial-mean absolute WTD error averaged across the 12 test segments, and panels (b–d) show the same metric for Segments 6, 9, and 12, respectively. The baseline model was trained using the unperturbed WY2020–WY2021 ParFlow-CLM simulations, whereas the augmented models additionally used samples generated from precipitation-perturbed WY2020–WY2021 simulations. Red annotations in panels (b–d) report the mean (μ_P) and standard deviation (σ_P) of domain-mean hourly precipitation within the respective segments.

At the segment level, augmentation was most beneficial when the added training samples were relevant to the precipitation conditions encountered during prediction. In Segment 6 (**Figure 7b**), which experienced intermediate precipitation activity, All-1.4× performed similarly to the baseline, whereas Dry-1000 increased the error. In the precipitation-active Segment 9 (**Figure 7c**), All-1.4× reduced the mean error, E_i, from 0.141 to 0.095 m, and the ModHeavy-1000 and Heavy-all strategies also outperformed the baseline. By contrast, Dry-1000 produced the largest error in this segment. Segment 12 (**Figure 7d**) exhibited the opposite behavior under relatively weak precipitation forcing: the baseline and Dry-1000 performed similarly, whereas the strategies emphasizing stronger precipitation regimes increased the error. Thus, no single augmentation strategy consistently improved prediction across all segments.

To examine this regime dependence more directly, the hourly error increments, $\Delta E_{i,t}$, from all 12 segments were pooled and stratified according to the precipitation regime of the corresponding 24 h windows (**Figure 8**). Under Heavy-regime windows, ModHeavy-1000 and Heavy-all shifted the mean $\Delta E_{i,t}$ from positive baseline values to negative values, indicating that the error decreased, on average, relative to the preceding hour. For Dry-regime windows, Dry-1000 also reduced the mean $\Delta E_{i,t}$ relative to the baseline, although its overall mean error, E, remained higher than that of the baseline (**Figure 7a**). Regime-specific augmentation may therefore improve error propagation without necessarily producing a lower error over the complete rollout.

Together, these results demonstrate that process-consistent data augmentation is potentially useful, but its benefit depends on the correspondence between the hydrological transitions represented in the augmented training data and those encountered during prediction. More broadly, the results indicate that augmentation should target underrepresented hydrological transitions rather than simply increase the total number of training samples. Models trained to emphasize Dry, Moderate, or Heavy precipitation conditions could be selected or combined according to the anticipated forcing regime. For operational groundwater prediction and water-resources management, this regime dependence also suggests a possible multi-model or regime-adaptive framework rather than reliance on a single universally augmented model.

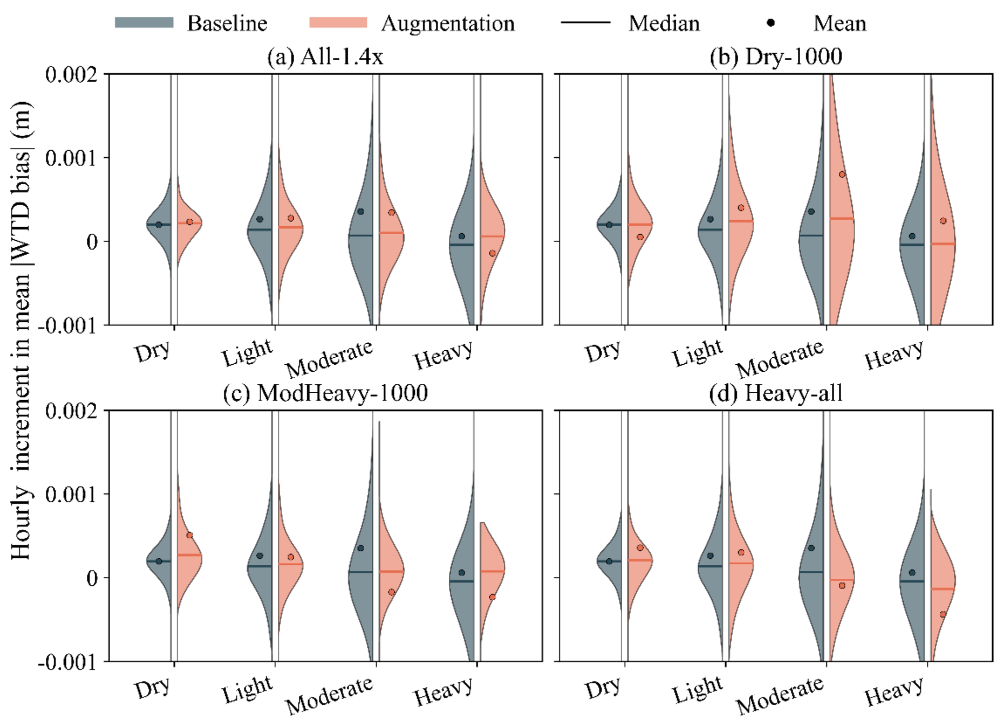

Figure 8. Effects of precipitation-regime data augmentation on hourly changes in WTD prediction error. Panels (a–d) compare the baseline model with models trained using the All-1.4×, Dry-1000, ModHeavy-1000, and Heavy-all augmentation strategies, respectively. Within each panel, the distributions are stratified into Dry, Light, Moderate, and Heavy precipitation regimes. The distributions were calculated from the 12 test segments of the unperturbed WY2019 simulation. Precipitation regimes were assigned using consecutive, non-overlapping 24 h windows classified according to domain-mean accumulated precipitation (P_{24}). The hourly error increment was defined as $\Delta E_{i,t} = E_{i,t} - E_{i,t-1}$, where $E_{i,t}$ denotes the spatial-mean absolute WTD error for segment i at prediction hour t. Positive and negative values indicate increases and decreases in error relative to the preceding hour, respectively. Gray and orange violins represent the baseline and augmented models, respectively, while horizontal lines and points indicate the median and mean.

6. Conclusions

This study systematically evaluated a groundwater-adapted PredFormer as a distributed surrogate for regional ParFlow-CLM simulations. The evaluation focused on long-horizon autoregressive prediction, the contributions and fusion of dynamic and static information, comparison with a recurrent reference model, and process-consistent data augmentation for different precipitation regimes. The adapted model generated continuous 720 h predictions of distributed multilayer pressure-head fields without introducing ParFlow-CLM reference states for correction after initialization.

Across the 720 h test segments, prediction errors generally increased with lead time but exhibited distinct temporal and spatial patterns. Larger upper-tail spatial errors were more closely associated with segment-scale precipitation amount and variability, whereas pronounced fluctuations in the error trajectories frequently coincided with abrupt wet–dry transitions. PredRNN was more accurate during the early prediction period, but PredFormer achieved lower and more stable errors over longer autoregressive horizons. These results suggest that the benefit of the Transformer architecture emerged primarily over extended autoregressive horizons rather than during the initial prediction period.

The contribution of additional inputs depended strongly on groundwater depth. Prescribed PME was the most influential additional input overall, reducing the mean absolute WTD error from 0.151 to 0.099 m relative to pressure head alone. Its contribution was greatest in shallow-WTD areas, whereas static hydrogeological attributes were most beneficial in the intermediate WTD zone. For WTD greater than 20 m, pressure head alone produced the lowest error, indicating that the antecedent groundwater state contained more useful predictive information than the additional short-term surface forcing or explicit static attributes over the evaluated horizon. The method used to integrate static information had a smaller but systematic influence. Post-temporal–spatial cross-attention achieved the lowest overall error and reduced the final 720 h error by 10.2% relative to direct raw-static concatenation. This result supports a fusion sequence in which temporal evolution and spatial interactions are first encoded and the resulting dynamic representation is subsequently conditioned on static attributes.

Process-consistent data augmentation produced relatively small changes in overall average error but clear precipitation-regime-dependent effects. Adding Moderate–Heavy or Heavy samples reduced hourly error accumulation under Heavy-precipitation conditions, whereas Dry augmentation reduced error accumulation during Dry conditions without consistently lowering the absolute WTD error over the complete prediction horizon. These findings indicate that augmentation should be designed to improve the representation of underrepresented hydrological transitions rather than simply increase the total number of training samples. They also suggest the potential value of regime-adaptive or multi-model prediction frameworks in which models trained for different hydrological conditions are selected or combined according to anticipated forcing regimes.

The present evaluation is limited to one regional basin, a three-year simulation record, and a 720 h prediction horizon. Because the model was developed as a surrogate for ParFlow, the current analysis focuses on its ability to emulate simulated groundwater dynamics. Future work should evaluate its transferability across basins and hydroclimatic conditions, examine longer training records and prediction horizons, and investigate whether groundwater data assimilation can improve state initialization and constrain long-horizon prediction errors. Extending the present offline framework toward the use of forecast forcing or interactive coupling with land-surface models would further clarify its operational applicability. Nevertheless, this study provides a systematic basis for understanding when Transformer-based groundwater surrogates are most effective and how input composition, static-information fusion, groundwater depth, and training-sample coverage influence their performance. These findings provide practical guidance for developing computationally efficient tools for regional groundwater prediction and water-resources management.

Code and data availability

The source code for training and evaluating the groundwater surrogate models is available at https://github.com/HH12138666/ParFlow-transformer. The version used in this study is permanently archived on Zenodo at https://doi.org/10.5281/zenodo.22145194. The unperturbed ParFlow-CLM simulation data used to construct the baseline surrogate-model dataset are available from Science Data Bank at https://doi.org/10.57760/sciencedb.46348. The precipitation-perturbed ParFlow-CLM simulations used for data augmentation, together with the trained model checkpoints and scripts for data analysis and figure generation, are available at https://doi.org/10.57760/sciencedb.0106u.

References

Alzubaidi, L., Zhang, J., Humaidi, A. J., Al-Dujaili, A., Duan, Y., Al-Shamma, O., Santamaría, J., Fadhel, M. A., Al-Amidie, M., and Farhan, L.: Review of deep learning: concepts, CNN architectures, challenges, applications, future directions, Journal of big Data, 8, 53, 2021.

Bennett, A., Tran, H., De la Fuente, L., Triplett, A., Ma, Y., Melchior, P., Maxwell, R. M., and Condon, L. E.: Spatio-Temporal Machine Learning for Regional to Continental Scale Terrestrial Hydrology, J Adv Model Earth Sy, 16, e2023MS004095, https://doi.org/10.1029/2023MS004095, 2024.

Bi, K., Xie, L., Zhang, H., Chen, X., Gu, X., and Tian, Q.: Accurate medium-range global weather forecasting with 3D neural networks, Nature, 619, 533-538, 10.1038/s41586-023-06185-3, 2023.

Bodnar, C., Bruinsma, W. P., Lucic, A., Stanley, M., Allen, A., Brandstetter, J., Garvan, P., Riechert, M., Weyn, J. A., Dong, H., Gupta, J. K., Thambiratnam, K., Archibald, A. T., Wu, C. C., Heider, E., Welling, M., Turner, R. E., and Perdikaris, P.: A foundation model for the Earth system, Nature, 641, 1180-1187, 10.1038/s41586-025-09005-y, 2025.

Chen, L., Zhang, D., Xu, J., Zhou, Z., Jin, J., Luan, J., and Wulamu, A.: Enhancing the accuracy of groundwater level prediction at different scales using spatio-temporal graph convolutional model, Earth Science Informatics, 18, 10.1007/s12145-025-01741-z, 2025.

Dai, T., Maher, K., and Perzan, Z.: Machine learning surrogates for efficient hydrologic modeling: Insights from stochastic simulations of managed aquifer recharge, Journal of Hydrology, 652, 10.1016/j.jhydrol.2024.132606, 2025.

Dosovitskiy, A., Beyer, L., Kolesnikov, A., Weissenborn, D., Zhai, X., Unterthiner, T., Dehghani, M., Minderer, M., Heigold, G., and Gelly, S.: An image is worth 16x16 words: Transformers for image recognition at scale, arXiv preprint arXiv:2010.11929, 2020.

Engdahl, N. B.: Impacts of Uncertain Permeability Fields on the Transient Hydrologic Response in Coupled Surface-Subsurface Simulations of a Headwaters Catchment, Water Resources Research, 61, 10.1029/2025wr040668, 2025.

Gao, Z., Shi, X., Wang, H., Zhu, Y., Wang, Y. B., Li, M., and Yeung, D.-Y.: Earthformer: Exploring space-time transformers for earth system forecasting, Advances in Neural Information Processing Systems, 35, 25390-25403, 2022.

Hersbach, H., Bell, B., Berrisford, P., Hirahara, S., Horányi, A., Muñoz-Sabater, J., Nicolas, J., Peubey, C., Radu, R., Schepers, D., Simmons, A., Soci, C., Abdalla, S., Abellan, X., Balsamo, G., Bechtold, P., Biavati, G., Bidlot, J., Bonavita, M., De Chiara, G., Dahlgren, P., Dee, D., Diamantakis, M., Dragani, R., Flemming, J., Forbes, R., Fuentes, M., Geer, A., Haimberger, L., Healy, S., Hogan, R. J., Hólm, E., Janisková, M., Keeley, S., Laloyaux, P., Lopez, P., Lupu, C., Radnoti, G., de Rosnay, P., Rozum, I., Vamborg, F., Villaume, S., and Thépaut, J. N.: The ERA5 global reanalysis, Quarterly Journal of the Royal Meteorological Society, 146, 1999-2049, 10.1002/qj.3803, 2020.

Jesse, G., Boateng, C. D., Aryee, J. N. A., Osei, M. A., Wemegah, D. D., Gidigasu, S. S. R., Britwum, A., Afful, S. K., Touré, H., Mensah, V., and Owusu-Afriyie, P.: A systematic review of machine learning models for groundwater level prediction, Applied Computing and Geosciences, 28, 10.1016/j.acags.2025.100303, 2025.

Kochkov, D., Yuval, J., Langmore, I., Norgaard, P., Smith, J., Mooers, G., Klöwer, M., Lottes, J., Rasp, S., Düben, P., Hatfield, S., Battaglia, P., Sanchez-Gonzalez, A., Willson, M., Brenner, M. P., and Hoyer, S.: Neural general circulation models for weather and climate, Nature, 632, 1060-1066, 10.1038/s41586-024-07744-y, 2024.

Kollet, S. J. and Maxwell, R. M.: Integrated surface–groundwater flow modeling: A free-surface overland flow boundary condition in a parallel groundwater flow model, Advances in Water Resources, 29, 945-958, 10.1016/j.advwatres.2005.08.006, 2006.

Kollet, S. J. and Maxwell, R. M.: Capturing the influence of groundwater dynamics on land surface processes using an integrated, distributed watershed model, Water Resources Research, 44, 2008.

Kratzert, F., Klotz, D., Brenner, C., Schulz, K., and Herrnegger, M.: Rainfall–runoff modelling using Long Short-Term Memory (LSTM) networks, Hydrology and Earth System Sciences, 22, 6005-6022, 10.5194/hess-22-6005-2018, 2018.

Leonarduzzi, E., Tran, H., Bansal, V., Hull, R. B., De la Fuente, L., Bearup, L. A., Melchior, P., Condon, L. E., and Maxwell, R. M.: Training machine learning with physics-based simulations to predict 2D soil moisture fields in a changing climate, Frontiers in Water, 4, 10.3389/frwa.2022.927113, 2022.

Li, X., Peng, C., Zhao, Y., and Xia, X.: A Hybrid DSCNN-GRU Based Surrogate Model for Transient Groundwater Flow Prediction, Applied Sciences, 15, 10.3390/app15084576, 2025.

Liesch, T. and Ohmer, M.: Strategies for incorporating static features into global deep learning models, Hydrol. Earth Syst. Sci., 30, 1877-1890, 10.5194/hess-30-1877-2026, 2026.

Liu, J., Shen, C., O'Donncha, F., Song, Y., Zhi, W., Beck, H. E., Bindas, T., Kraabel, N., and Lawson, K.: From RNNs to Transformers: benchmarking deep learning architectures for hydrologic prediction, Hydrology and Earth System Sciences, 29, 6811-6828, 10.5194/hess-29-6811-2025, 2025.

Maxwell, R. M. and Kollet, S. J.: Interdependence of groundwater dynamics and land-energy feedbacks under climate change, Nature Geoscience, 1, 665-669, 10.1038/ngeo315, 2008.

Maxwell, R. M. and Miller, N. L.: Development of a coupled land surface and groundwater model, Journal of Hydrometeorology, 6, 233-247, 2005.

Maxwell, R. M., Condon, L. E., and Melchior, P.: A Physics-Informed, Machine Learning Emulator of a 2D Surface Water Model: What Temporal Networks and Simulation-Based Inference Can Help Us Learn about Hydrologic Processes, Water, 13, 10.3390/w13243633, 2021.

Muñoz-Sabater, J., Dutra, E., Agustí-Panareda, A., Albergel, C., Arduini, G., Balsamo, G., Boussetta, S., Choulga, M., Harrigan, S., and Hersbach, H.: ERA5-Land: A state-of-the-art global reanalysis dataset for land applications, Earth system science data discussions, 2021, 1-50, 2021.

Nguyen, T., Brandstetter, J., Kapoor, A., Gupta, J. K., and Grover, A.: ClimaX: A foundation model for weather and climate, International Conference on Machine Learning,

Rasiya Koya, S. and Roy, T.: Temporal Fusion Transformers for streamflow Prediction: Value of combining attention with recurrence, Journal of Hydrology, 637, 10.1016/j.jhydrol.2024.131301, 2024.

Rasp, S., Dueben, P. D., Scher, S., Weyn, J. A., Mouatadid, S., and Thuerey, N.: WeatherBench: A Benchmark Data Set for Data-Driven Weather Forecasting, Journal of Advances in Modeling Earth Systems, 12, 10.1029/2020ms002203, 2020.

Reichstein, M., Camps-Valls, G., Stevens, B., Jung, M., Denzler, J., Carvalhais, N., and Prabhat: Deep learning and process understanding for data-driven Earth system science, Nature, 566, 195-204, 10.1038/s41586-019-0912-1, 2019.

Shazeer, N.: Glu variants improve transformer, arXiv preprint arXiv:2002.05202, 2020.

Sun, A., Tang, Z., Zheng, C., Shangguan, W., and Yang, C.: What Can We Learn from a Reduced-Dimensional Groundwater Representation for Diagnosing Groundwater–Land Interactions? Insights from the Water Table Ratio, EGUsphere, 2026, 1, 2026.

Sun, X., Zhong, X., Xu, X., Huang, Y., Li, H., Neelin, J. D., Chen, D., Feng, J., Han, W., Wu, L., and Qi, Y.: A data-to-forecast machine learning system for global weather, Nature Communications, 16, 10.1038/s41467-025-62024-1, 2025.

Tang, Y., Qi, L., Li, X., Ma, C., and Yang, M.-H.: Video prediction transformers without recurrence or convolution, arXiv preprint arXiv:2410.04733, 2024.

Taylor, R. G., Scanlon, B., Döll, P., Rodell, M., van Beek, R., Wada, Y., Longuevergne, L., Leblanc, M., Famiglietti, J. S., Edmunds, M., Konikow, L., Green, T. R., Chen, J., Taniguchi, M., Bierkens, M. F. P., MacDonald, A., Fan, Y., Maxwell, R. M., Yechieli, Y., Gurdak, J. J., Allen, D. M., Shamsudduha, M., Hiscock, K., Yeh, P. J. F., Holman, I., and Treidel, H.: Ground water and climate change, Nature Climate Change, 3, 322-329, 10.1038/nclimate1744, 2012.

Tran, H., Leonarduzzi, E., De la Fuente, L., Hull, R. B., Bansal, V., Chennault, C., Gentine, P., Melchior, P., Condon, L. E., and Maxwell, R. M.: Development of a Deep Learning Emulator for a Distributed Groundwater–Surface Water Model: ParFlow-ML, Water, 13, 3393, 2021.

Van Genuchten, M. T.: A closed-form equation for predicting the hydraulic conductivity of unsaturated soils, Soil science society of America journal, 44, 892-898, 1980.

Vaswani, A., Shazeer, N., Parmar, N., Uszkoreit, J., Jones, L., Gomez, A. N., Kaiser, Ł., and Polosukhin, I.: Attention is all you need, Proceedings of the 31st International Conference on Neural Information Processing Systems, Long Beach, California, USA2017.

Wang, Y., Long, M., Wang, J., Gao, Z., and Yu, P. S.: Predrnn: Recurrent neural networks for predictive learning using spatiotemporal lstms, Advances in neural information processing systems, 30, 879–888, 2017.

Xu, W., Chen, J., and Corzo, G.: Combining data augmentation and hybrid modeling approaches for deep learning-based monthly streamflow forecasting, Journal of Hydrology, 659, 10.1016/j.jhydrol.2025.133318, 2025.

Yang, C., Huang, H., Tang, Z., Dai, Y., and Chang, X.: A hybrid physics–ML framework for integrating groundwater dynamics into land surface modeling, EGUsphere, 2026, 1, 2026a.

Yang, C., Sun, A., Zhang, S., Dai, Y., Kollet, S., and Maxwell, R.: 20 years of trials and insights: bridging legacy and next generation in ParFlow and Land Surface Model Coupling, Geosci. Model Dev., 19, 1849-1866, 10.5194/gmd-19-1849-2026, 2026b.

Yang, C., Jia, Z., Xu, W., Wei, Z., Zhang, X., Zou, Y., McDonnell, J., Condon, L., Dai, Y., and Maxwell, R.: CONCN: a high-resolution, integrated surface water–groundwater ParFlow modeling platform of continental China, Hydrology and Earth System Sciences, 29, 2201-2218, 10.5194/hess-29-2201-2025, 2025.

Supplementary Information

Text S1. Detailed Formulation and Implementation of the Groundwater-Adapted PredFormer

This section retains the standard PredFormer formulations that support the concise main-text framework description. Supplementary Methods S1.1-S1.3 provide patch tokenization and positional encoding, Gated Transformer Blocks, and temporal-first factorized attention, respectively. Groundwater-specific static fusion, residual prediction, blockwise autoregression, loss calculation, window reconstruction, and training settings are described in the main text.

S1.1 Patch Tokenization and Positional Encoding

To reduce GPU memory usage, the gridded pressure and forcing fields were processed in local spatial windows rather than as a single domain-wide Transformer input. Adjacent windows overlapped to retain spatial context across partition boundaries and reduce boundary artifacts in the reconstructed fields. Each window was then divided into non-overlapping p × p patches. At time *t*, the n-th patch was flattened and linearly projected as:

$$z_{t,n} = W_e vec\left(x_{t,n}\right) + b_e + e_{t,n}.$$

Here, W_e and b_e are learnable embedding parameters, and $e_{t,n}$ encodes the temporal and spatial position of the patch. The resulting representation for each local window is

$$Z \in \mathbb{R}^{B \times T \times N \times D},$$

where B is the batch size, T is the input length, N is the number of spatial patches per time step, and D is the token dimension. We used 80 × 64 windows with strides of 40 and 32, respectively. With a patch of 8 × 8 = 64 grid cells, each time step was represented by 8 × 10 = 80 spatial tokens.

S1.2 Gated Transformer Blocks

Within each GTB, multi-head self-attention is used to extract dependencies among tokens. A single attention head is defined as:

$$\text{Attention}(Q, K, V) = \text{Softmax}\left(\frac{QK^T}{\sqrt{d_k}}\right)V,$$

where Q, K, and V are the query, key, and value projections of the input tokens, respectively, and the head dimension scales the attention scores. The outputs from multiple attention heads are concatenated and linearly mapped to form multi-head self-attention. The feed-forward component uses the SwiGLU gating structure adopted in PredFormer:

$$\text{SwiGLU}(x) = W_2\left[\text{SiLU}(W_g x + b_g) \odot (W_z x + b_z)\right] + b_2,$$

where $x \in \mathbb{R}^D$ denotes an input token, $\odot$ denotes element-wise multiplication, and SiLU denotes the sigmoid linear unit activation function. The matrices W_g, W_z, and W_2 are learnable weights, and b_g, b_z, and b_2 are learnable bias vectors. The l-th GTB is written as:

$$Y^l = Z^l + \mathrm{DropPath}\{\mathrm{MSA}[\mathrm{LN}(Z^l)]\},$$

$$Z^{l+1} = Y^l + \mathrm{DropPath}\{\mathrm{SwiGLU}[\mathrm{LN}(Y^l)]\},$$

where MSA denotes multi-head self-attention and LN denotes layer normalization. Z^l, Y^l, and Z^{l+1} denote the input, post-attention representation, and output of the l-th GTB, respectively. Residual connections facilitate gradient propagation, and DropPath regularizes the network during training.

Within the factorized PredFormer encoder, temporal GTBs apply self-attention across the input-time tokens for each spatial patch, whereas spatial GTBs apply self-attention across the spatial-patch tokens at each time step.

S1.3 Temporal-First Factorized Attention

A temporal-first factorized encoder was used to reduce the computational cost of full spatiotemporal attention while retaining separate temporal and spatial feature extraction. The model first applies temporal attention to each spatial patch across the input time steps and then applies spatial attention across patches at each time step:

$$H = T_S[T_T(Z)],$$

where Z is the input token representation, H is the output representation, and T_T and T_S denote the temporal and spatial Transformer encoders, respectively.

For temporal attention, the token tensor is rearranged such that the T tokens associated with each spatial patch form an attention sequence. The temporal encoder therefore learns the evolution of each local pressure-forcing representation over the input period. The resulting tokens are then rearranged such that the N spatial-patch tokens at each time step form an attention sequence for the spatial encoder. This operation enables the model to capture spatial dependencies among local groundwater states and auxiliary forcing representations.

Each encoder contains six GTBs. By decomposing attention over all $T \times N$ spatiotemporal tokens into separate temporal and spatial operations, the factorized design reduces the attention cost for large gridded groundwater fields.

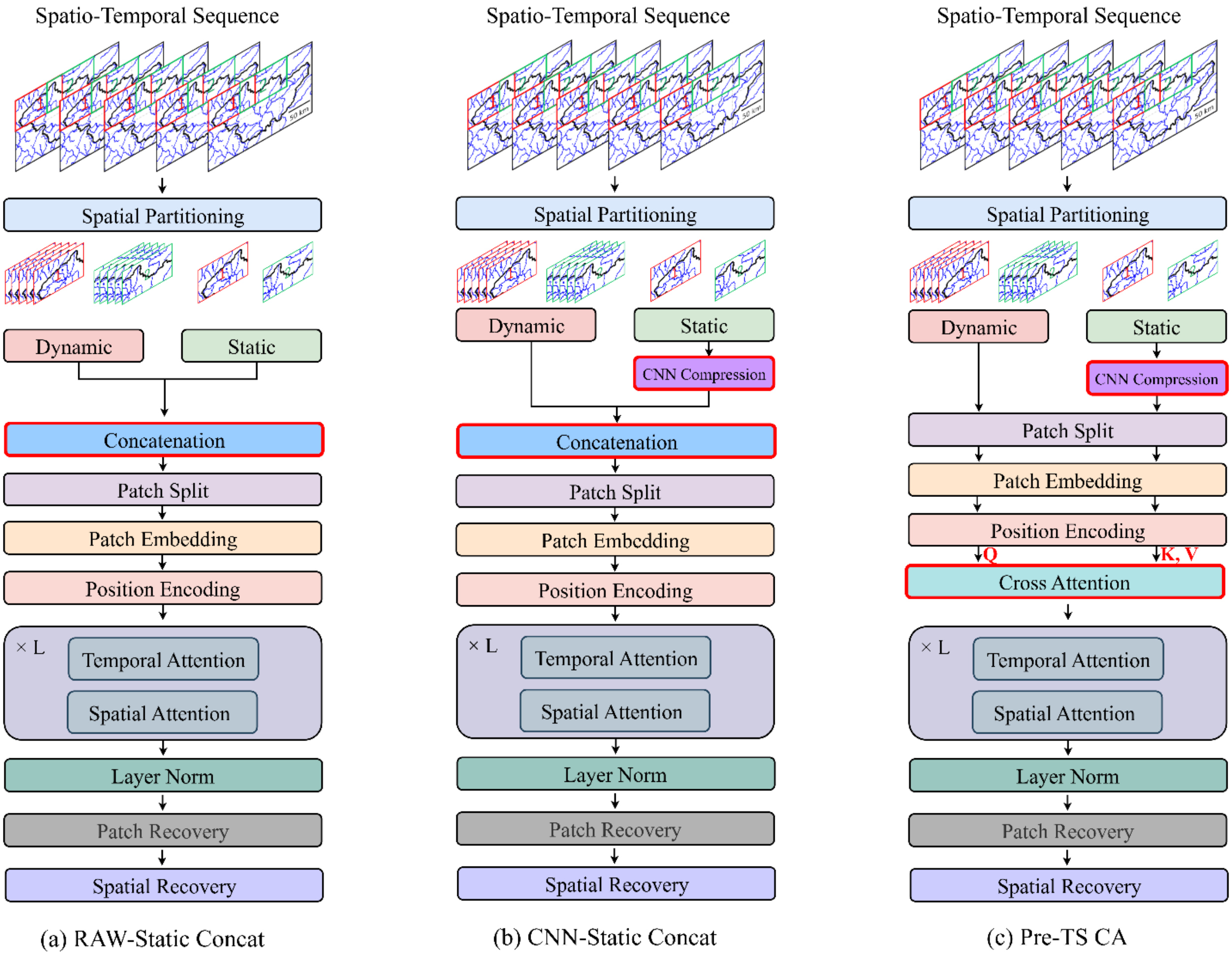

Figure S1. Alternative dynamic–static fusion architectures used for architecture screening. Panel (a) shows RAW-Static Concatenation, in which the original static attributes are concatenated with the dynamic inputs before patch tokenization. Panel (b) shows CNN-Static Concatenation, in which the static attributes are first compressed using a convolutional encoder and then concatenated with the dynamic inputs. Panel (c) shows Pre-TS CA, in which CNN-compressed static tokens are fused with dynamic tokens through cross-attention before temporal–spatial Transformer encoding. All structures use the same dynamic PredFormer backbone. The Post-TS CA configuration used in the main experiments is shown in Figure 2.

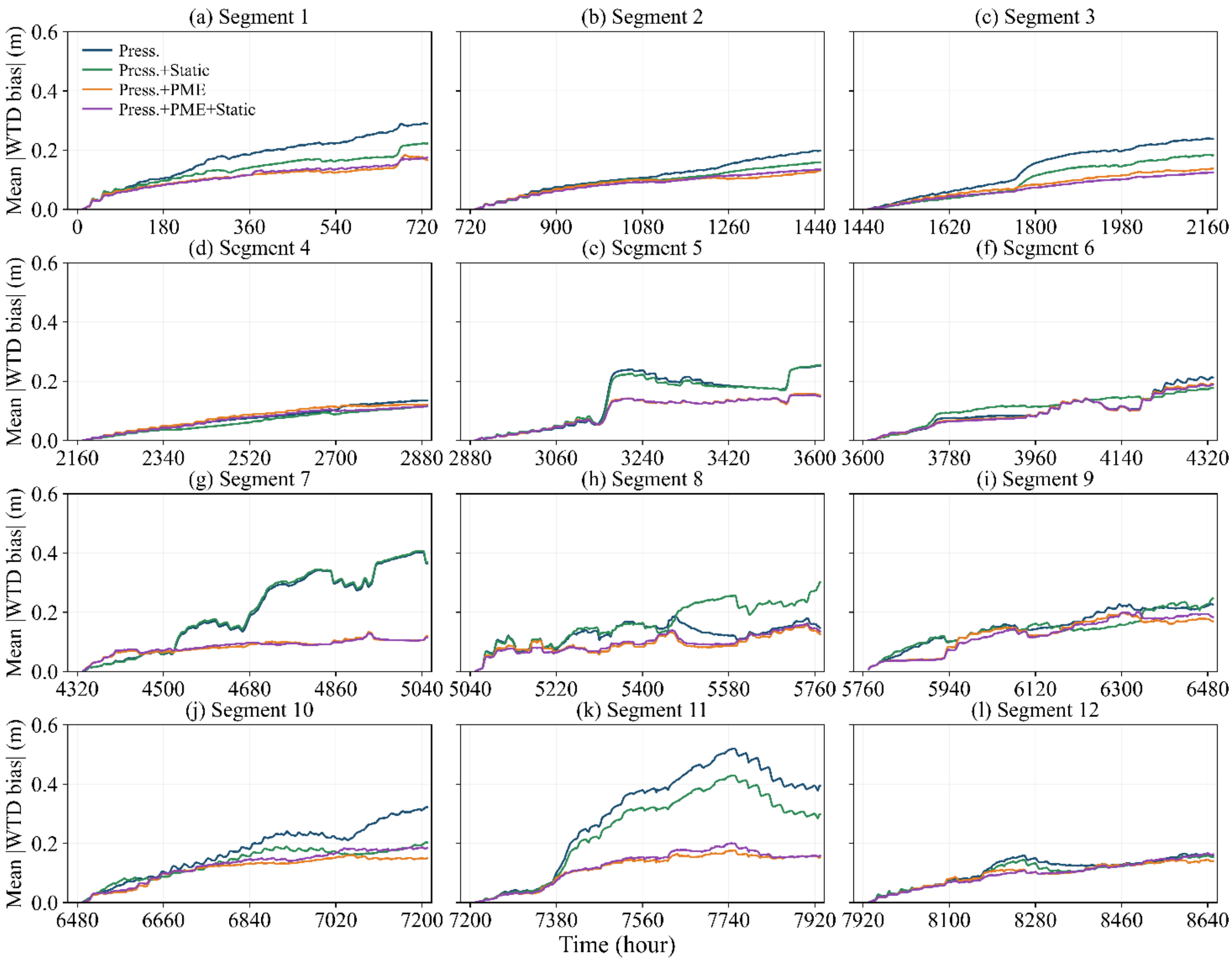

Figure S2. Segment-wise effects of input composition on 720 h autoregressive WTD prediction. Panels (a–l) show the 12 independently initialized rollout segments from the independent WY2021 test simulation. Curves represent pressure head only, pressure head with prescribed PME forcing, pressure head with static attributes, and pressure head with both prescribed PME forcing and static attributes. Each segment was initialized using 12 h of ParFlow-CLM reference pressure; thereafter, predicted pressure fields were recursively used as inputs without reference-state correction. The error at each forecast hour is the spatial mean absolute WTD error. P denotes pressure head, PME denotes prescribed layer-resolved P−ET source–sink forcing, and S denotes static hydrogeological attributes.

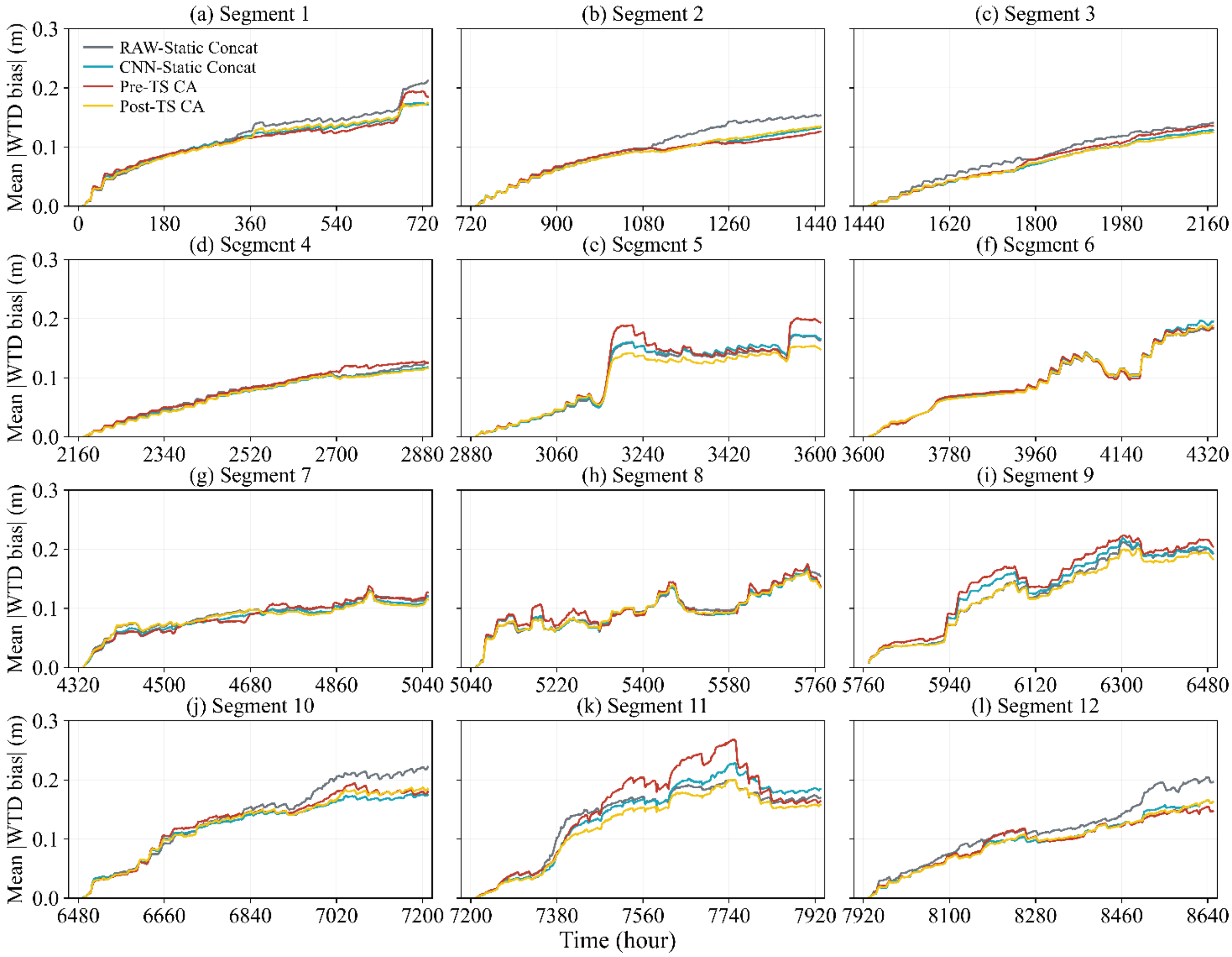

Figure S3. Segment-wise effects of dynamic–static fusion strategy on 720 h autoregressive WTD prediction. Panels (a–l) show the 12 independently initialized rollout segments from the independent WY2021 test simulation. The curves represent RAW-Static Concatenation, CNN-Static Concatenation, Pre-TS CA, and Post-TS CA. All configurations used the same dynamic inputs, static attributes, data split, and training procedure. Each segment was initialized using 12 h of ParFlow-CLM reference pressure, after which no reference pressure was supplied for state correction. The error at each forecast hour is the spatial mean absolute WTD error. The fusion strategies are defined in Figure 2 and Supplementary Figure S1.

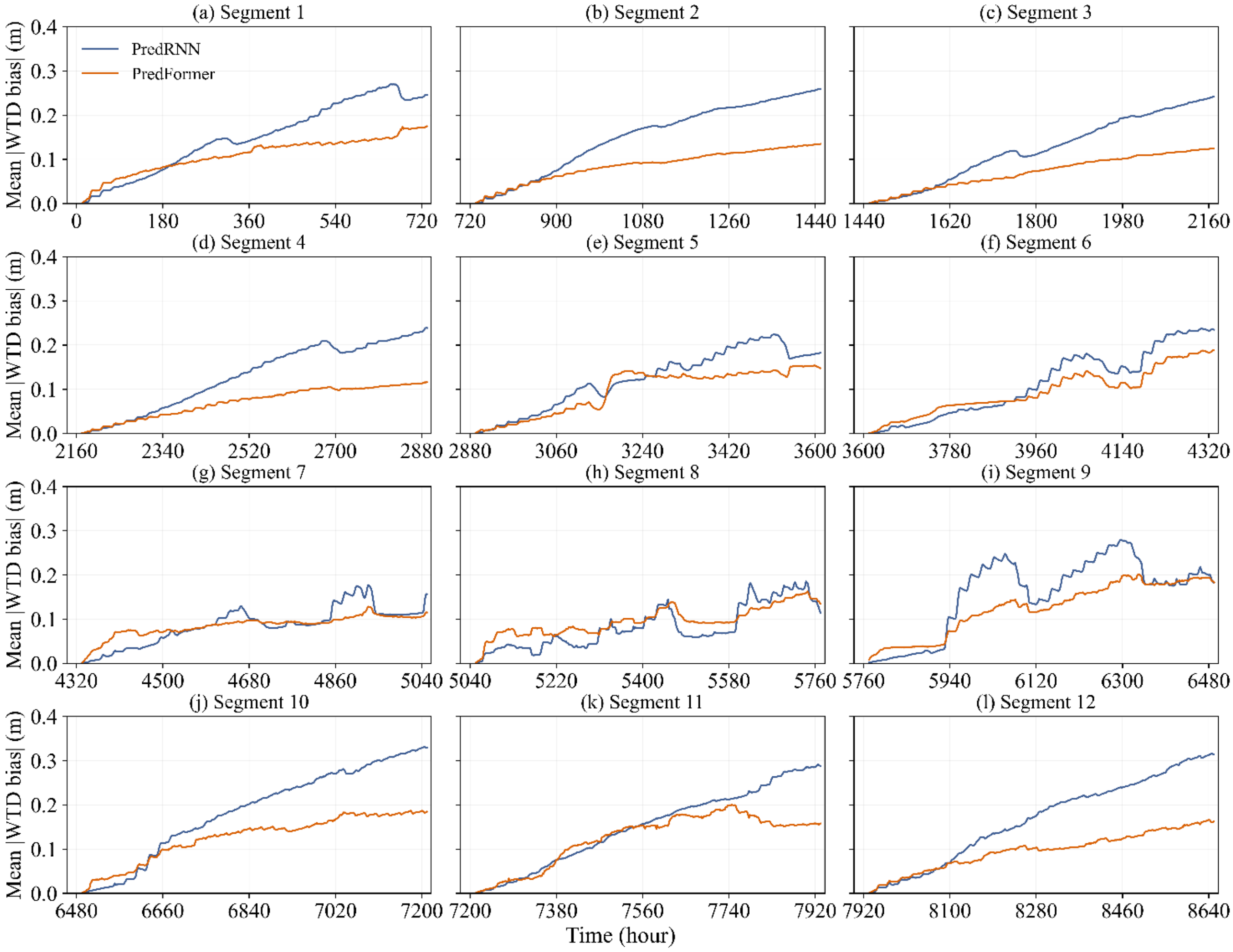

Figure S4. Segment-wise comparison between PredFormer and PredRNN during 720 h autoregressive WTD prediction. Panels (a–l) correspond to the 12 independently initialized rollout segments from the independent WY2021 test simulation. Each curve shows the spatial-mean absolute WTD error at each prediction hour. Both models were trained using the same data split, forecast origins, target pressure fields, prescribed PME fields, and static attributes. PredFormer was initialized using a 12 h reference-pressure sequence and generated 12 h pressure blocks, whereas PredRNN used the final pressure field from the same initialization period and generated pressure fields sequentially at hourly time steps. No reference pressure was supplied for state correction after initialization.

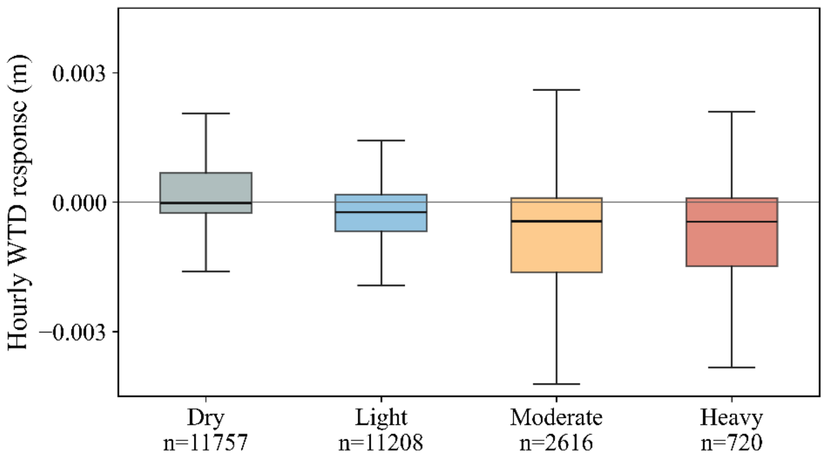

Figure S5. Hourly WTD response across precipitation regimes in the ParFlow-CLM reference simulations. The hourly response was calculated as $\Delta\mathrm{WTD} = \mathrm{WTD}(t) - \mathrm{WTD}(t-1)$ using consecutive hourly outputs from WY2019–WY2021. Because WTD is defined as depth below the land surface, negative $\Delta\mathrm{WTD}$ indicates a shallower water table, whereas positive values indicate a deeper water table. Precipitation regimes were classified from 24 h domain-mean accumulated precipitation sample windows. Boxes show the interquartile range, center lines show the median, and whiskers show the non-outlier range. n denotes the number of hourly WTD-response samples in each regime.

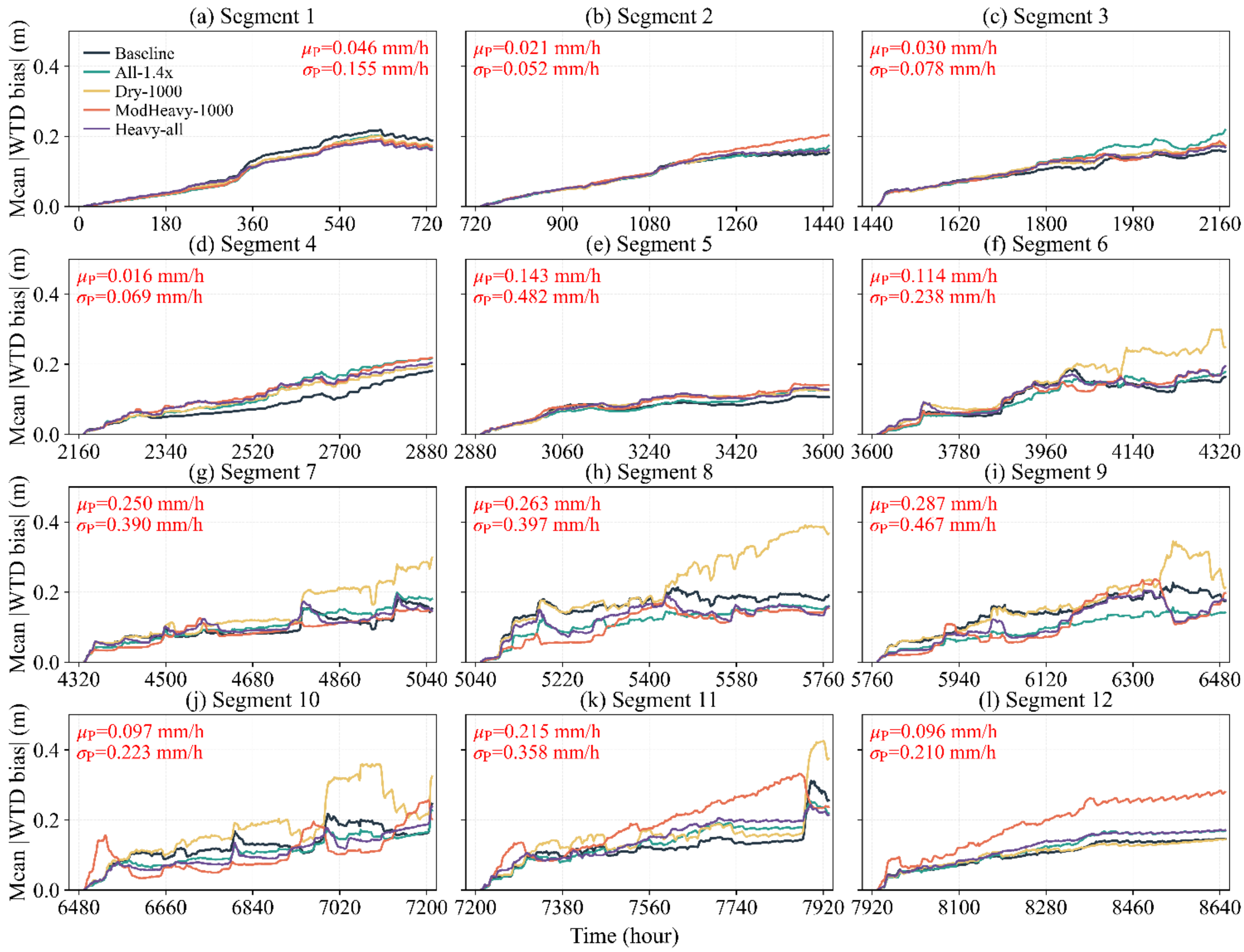

Figure S6. Segment-wise effects of precipitation-regime augmentation on 720 h autoregressive WTD prediction. Panels (a–l) show the 12 independent rollout segments from the independent WY2019 test simulation. Each curve represents the spatial-mean absolute WTD error. The baseline model was trained using regular WY2020–WY2021 ParFlow-CLM simulations, whereas the augmented models used the same training data supplemented with precipitation-perturbed WY2020–WY2021 simulations. No WY2019 samples were used for training. The augmentation strategies are defined in Table 2. Red annotations indicate the mean μ_P and standard deviation σ_P of hourly precipitation within each 720 h rollout segment, representing the average precipitation intensity and temporal variability during the prediction period.